Magma chamber-related transition from magmatic to solid-state fabrics within the Late Triassic granitic Dushan pluton (North China)

Huabiao Qiu, Wei Lin, Yan Chen, Michel Faure, Lingtong Meng, Zhiheng Ren, Jipei Zeng, Quanlin Hou

Magma chamber-related transition from magmatic to solid-state fabrics within the Late Triassic granitic Dushan pluton (North China)

Huabiao Qiu[1,2,3,4], Wei Lin[1,3]*, Yan Chen[2], Michel Faure[2], Lingtong Meng[1,3], Zhiheng Ren[1,3], Jipei Zeng[1,3], and Quanlin Hou[3]

[1]State Key Laboratory of Lithospheric Evolution, Institute of Geology and Geophysics, Chinese Academy of Sciences/Innovation Academy for Earth Science, Chinese Academy of Sciences, Beijing 100029, China

[2]Univ. Orléans, CNRS, BRGM, ISTO, UMR 7327, F-45071, Orléans, France

[3]College of Earth and Planetary Sciences, University of Chinese Academy of Sciences, Beijing 100049, China

[4]Petroleum Exploration and Production Research Institute, SINOPEC, Beijing 100083, China

*Corresponding author: (linwei@mail.iggcas.ac.cn)

SUMMARY

Penetrative petro-fabrics in plutons, particularly late-stage solid-state fabrics, are usually considered to record regional tectonism. However, these fabrics are fundamentally ambiguous to correlate with magma-chamber processes or regional tectonics. Understanding the processes of fabric formation requires a proper understanding of pluton formation and emplacement mechanism. In this paper, we provide a case study of a transition from magma chamber-related magmatic to solid-state fabrics within the Late Triassic granitic Dushan pluton (North China) based on a multidisciplinary investigation of its emplacement mechanism, including structural

geology, isotope chronology, AMS data measurement, and gravity modeling. The Dushan pluton varies in a southwest direction from a megascopically isotropic monzogranite in the northeast to an arc-shaped gneissic monzogranite with locally mylonitic zones along the southwest margin. The compatible outward dipping mesoscopic and magnetic susceptibility foliations define a dome-like roof with a NE-SW long axis. Considering the absence of similar penetrative fabrics in the country rocks, a continuum of magma chamber-related fabric variations within the pluton, from magmatic to solid-state conditions, probably formed during pluton emplacement. Gravity modeling suggests that the Dushan pluton has a NE-SW trending tongue-like shape with a northeast positioned root. We propose a model in which the Dushan pluton was emplaced through a northeast feeder zone, beginning probably as a sill then evolving by inflation via several magma batches. Later magma batches inflated the country rocks to form the final pluton. Magma inflation deformed the former semi-solid magma, forming a curved gneissic to mylonitic foliation along the southwest margin of the pluton. Several multidisciplinary studies show that the North China Craton (NCC) experienced a Late Triassic regional crustal extension attending the Dushan pluton emplacement. Both mesoscopic and magnetic susceptibility fabrics of the pluton could be more related to magmatic process rather than regional tectonics, implying that such fabrics within plutons need to be used with caution for inferring regional tectonics.

Keywords: Microstructure, Magnetic mineralogy and petrology, Magnetic fabrics and anisotropy, Pluton emplacement, Magma chamber processes

1 INTRODUCTION

During the emplacement of granitic plutons, magmatic fabrics can not only record mineral preferred orientation in the flowing magma but also preserve information on the strain field which acts on the magma (Paterson et al. 1989; Bouchez et al. 1997; Žák et al. 2012). Magmatic

fabrics usually reflect only the last increment of strain during crystallization, because magma flow can easily reset earlier fabrics (Paterson et al. 1998; Benn et al. 2001). These magmatic fabrics form in relation to a series of processes that reflect either the magma chamber-related dynamics or the response to a regional stress state to which the magma was subjected during final crystallization (Archanjo et al. 2002). The solid-state fabrics record structural deformation, which occurred after full crystallization of the magma (Paterson et al. 1989). Numerous studies have revealed the interplay between magma intrusive process and regional tectonics (e.g., Bouchez & Gleizes 1995; Gleizes et al. 1997; De Saint Blanquat et al. 2011; Žák et al. 2011). Consequently, fabric studies of granite plutons have been used for their potential to record the tectonic regime (i.e., compressional, extensional, and strike-slip) coeval with granitic emplacement (e.g., Hutton 1988; Paterson et al. 1989; Bouchez & Gleizes 1995; Žák et al. 2008; Qiu et al. 2020). The fabrics of most large-scale plutons usually reflect regional tectonic characteristics. For instance, several plutons in French Massif Central recorded the NW-SE to E-W regional extension during the Variscan orogenic collapse (e.g., Faure & Pons 1991; Talbot et al. 2000, 2004, 2005; Joly et al. 2009; Turrillot et al. 2011). However, a causal link between pluton emplacement and regional tectonics should be established carefully, because research requires the consistency of geometrical and spatio-temporal relationships with regional deformation (Paterson & Tobisch 1992; Zibra et al. 2012). Magmatic to solid-state fabrics are a typical feature of many concentrically zoned plutons, i.e., magmatic fabrics are preserved in the core and subsolidus fabrics in the periphery of pluton (Machek et al. 2019). These fabrics are considered to reflect several processes of magma emplacement: (1) amalgamation of successive small magma batches (Barboni et al., 2012; Stearns & Bartley, 2014); (2) increments of large magma batches (Machek et al. 2019); (3) a diapirically ascended pluton (Mahon et al., 1988);

and (4) syntectonic nested diapirs (Paterson & Vernon 1995). Yet whether these fabrics document regional tectonics or not should consider multiple factors, including (i) parallelism between pluton fabrics and solid-state fabrics in its host rocks (Paterson et al. 1998); and (ii) consistency of structural features related to shearing that affected a pluton and its country rocks (Blumenfeld & Bouchez 1988).

In the Late Triassic, the northern NCC was characterized by extensive surface uplift, voluminous magmatism, and intracontinental extension (Meng et al. 2020). Late Triassic alkaline complexes (e.g., quartz syenite, nepheline syenite, A-type granite, and mafic-ultramafic rocks) were widely emplaced into the northern NCC (Yang et al. 2012; Zhang et al. 2012; Figure 1). Detrital zircon dating and sedimentary studies suggest that the NCC was an extensional tectonic setting during the deposition of conformable Upper Triassic to Lower Jurassic strata in some remnant basins (e.g., the Niuyingzi-Dengzhangzi basin and the Xiabancheng basin; Davis et al. 2009; Meng et al. 2014; Figure 1c). The NE–SW regional extension is documented in the Sonid Zuoqi metamorphic core complex (224 ~ 208 Ma) in the adjacent Solonker zone (Davis et al. 2004; Figure 1b). The above evidence shows that the NCC experienced a phase of Late Triassic intracontinental extension. This hypothesis is also supported by a recent study on the Late Triassic Wangtufang pluton that reveals a NE–SW extension by the observed NE–SW striking magnetic lineations and dykes as tension gashes perpendicular to the magnetic lineations (Qiu et al. 2020; Figure 1c). Here we show that a continuum of fabrics that reflect magmatic to solid-state conditions within the Dushan pluton (North China) formed during emplacement. The consistency of the solid-state fabrics with emplacement kinematics inferred from well-defined magmatic structures and lack of kinematically compatible solid-state fabrics in the host rock show that late-stage solid-state fabrics in plutons may record evidence of early post-emplacement

regional tectonics, however, this is not the case in our study. We hypothesize that the fabrics of the Dushan pluton probably did not record regional tectonics and propose a magma chamber-related fabric development model using a multidisciplinary study, including structural geology, isotope chronology, AMS data measurement, and gravity modeling. Such fabrics within plutons need to be used with caution for inferring regional tectonics.

2 GEOLOGIC OVERVIEW OF THE NORTHERN NCC

After its Paleoproterozoic cratonization (Zhao et al. 2001), the NCC was characterized by a stable Proterozoic to Permian time of deposition of sedimentary rocks (Li et al. 2016). The geologic evolution of the northern NCC began in the late Paleozoic–early Mesozoic, resulting possibly from the closure of the Paleo-Asian Ocean (Davis et al. 2001; Xiao et al. 2003). The related deformation was featured by E–W trending ductile shearing (e.g., Chicheng-Fengning, Fengning-Longhua, and Damiao-Niangniangmiao ductile shear zones), and thrust faults and related folds (Wang et al. 2013; Figure 1). The late Paleozoic–early Mesozoic magmatism is widely developed in the northern NCC (Zhang et al. 2014; Figure 1c). During the Late Triassic, extensive surface uplift, voluminous magmatism, and rift basins occurred in the northern NCC, supporting the Late Triassic extensional tectonic setting of the northern NCC (Meng et al. 2020).

The Jurassic to Cretaceous intra-continental orogeny, traditionally referred to as the Yanshanian movement, is characterized by widely distributed NE- and E–W- trending fold and thrust belts and magmatism (e.g., Davis et al. 2001; Faure et al. 2012; Figure 1). The Yanshan fold-and-thrust belt generally trends E–W, but NE–SW in the east. Several generations of out-of-sequence thrusts developed during the Middle Jurassic to Cretaceous and crosscut preexisting southward verging E–W trending structures (Li et al. 2016). Several Jurassic to Cretaceous fault-bounded basins, related to multi-phase thrusting events, are widely distributed in the Yanshan

fold-and-thrust belt, whereas the Triassic strata are only exposed in some remnant basins (Figure 1).

During the Early Cretaceous, extensional tectonism, characterized by magmatism, rift basins, and metamorphic core complexes, became prevalent in the NCC and its adjacent regions (Lin & Wei 2018; Figure 1c).

3 FIELD OBSERVATIONS IN THE DUSHAN PLUTON

3.1 Principal rock types and Bulk Architecture

The Dushan pluton intrudes into the northeast part of the E–W trending Malanyu anticline (Figure 1). To the northeast of the Dushan pluton, the Dashizhu pluton consists mainly of granite and granodiorite (Ye et al. 2014; Xiong et al. 2017; Figure 2). The country rocks, composed of Archaean gneiss (Qianxi Group) and Neoproterozoic unmetamorphosed carbonate rocks (Changcheng group and Jixian group), are deformed by NE–SW striking fold-and-thrust belts (Figure 2). Around the Dushan pluton, the contact with the country rocks is sharp with a regular elliptical shape (Figures 2 and 3a). The foliations in the gneiss dip mainly at moderate to high angles to the NNW or SSE (Figure 3b). Some post-folial folds can be observed (Figure 3c). Close to the contact, the foliation of the gneiss is roughly parallel to the margin of the Dushan pluton (Figure 2). The arc-shaped fold-and-thrust belt, which is expressed on the northwest side of the Dushan pluton, and wraps along the elliptical-shaped contact of the pluton (Figure 3d).

3.2 Fabric and Structure of the Dushan Pluton

The Dushan pluton, which extends ~30 km along a NE-SW long axis, consists of monzogranite with a biotite-rich marginal facies (Figure 2; Ye et al. 2014; Jiang et al. 2018). There is no clear contact between these facies. Mineral fabrics are well-developed in the

southwest part of the Dushan pluton, whereas its central and northeast parts display only weak planar fabrics or appear isotropic (Figure 2 and 4a-4b). Quartz, K-feldspar, and plagioclase crystals have sub-euhedral to euhedral habitus. Biotite and amphibole are randomly distributed without any preferred orientation. The pluton varies from isotropic monzogranite in the northeast to arc-shaped gneissic monzogranite at the megascopic scale, with locally mylonitic zones in its southwest margin (Figure 2). The transition between gneissic, up to mylonitic fabrics, and isotropic fabrics is gradational without sharp contacts.

The southward increase in deformation fabric toward the pluton margin is illustrated by a fabric evolution, ranging from a poorly-defined foliation to a gneissic foliation, which strikes parallel to the pluton margin (Figures 2 and 4c-4d). The gneissic foliation is marked by oriented biotite platelets and K-feldspar megacrysts (Figures 2 and 4c-4d). Strongly flattened xenoliths of country rocks, parallel to the gneissic foliation, are common in the southwest border of the Dushan pluton (Figure 4d), without obvious stretching lineations. Close to the southeast contact with the country rocks, the foliation dips toward the interior of the pluton (Figure 2). This southwest part of the pluton also reveals a mylonitic fabric with a well-defined lineation that is locally well developed (Figures 2 and 4e-4f). The mylonite exhibits a margin-parallel foliation with NE-SW trending lineation outlined by plagioclase and K-feldspar crystals that consistently plunge 30°–40° to the southwest. A top-to-the-SW shearing was indicated by sigmoidal-shaped K-feldspars (Figure 4f). Similar mylonitic fabrics are not present in the host rocks close to the pluton.

4 MICROSCOPIC OBSERVATIONS

In the Dushan pluton, microscopic observations were made on rocks collected from the domains characterized by magmatic foliation to establish the magnetic fabric correlation with the

mineral fabrics. Based on observations of more than sixty thin sections, three microscopic fabric types have been identified in the Dushan pluton (Figure 5).

(1) Magmatic fabrics and weak solid-state fabrics. The magmatic fabrics are found in the northeast part of the Dushan pluton (Figures 5a and 5g). Quartz crystals are anhedral, non-deformed, and do not exhibit obvious shape preferred orientation (Figure 5a). However, a weak solid-state overprint is also commonly present in the Dushan pluton (Figures 5b and 5g). Millimeter-sized quartz grains show very weak undulose extinction. Sometimes, small-sized recrystallized quartz grains are distributed at the margin of coarse grains (Figure 5b) suggesting that they underwent slight dynamic recrystallization. The euhedral biotite crystals are neither kinked nor bent with a sharp extinction. Significant solid-state deformation is absent. Therefore, these weak solid-state fabrics are interpreted to have formed under submagmatic to solid-state flow at high-temperature subsolidus conditions.

(2) Moderate solid-state fabrics. Many samples from the southwest part and local areas of the northeast part of the Dushan pluton exhibit moderate solid-state fabrics. Quartz grains display intensive dynamic recrystallization and are replaced by aggregates of newly formed grains (Figures 5c-5d and 5g). Numerous subgrains, presenting serrated boundaries, show a conspicuous undulose extinction. Biotite grains are kinked and bent. Quartz grains are organized into ribbons and form a gneissic foliation. At this stage, the plagioclase and K-feldspars do not display any recrystallization or deformation, suggesting low-grade temperature conditions during deformation (300–400°C; Passchier & Trouw 2005).

(3) Strong solid-state microstructures. Near the southern border of the Dushan pluton, the monzogranite is locally mylonitic (Figures 5e-5g). Quartz aggregates presenting irregular boundaries record subgrain rotation, indicative of widespread recrystallization. Biotite

grains are commonly elongate, kinked, and bent but plagioclase grains and K-feldspars are devoid of ductile deformation. Extremely fine-grained quartz and feldspar sigma-type tails are found on K-feldspar and plagioclase residual phenoclasts, suggesting temperature conditions between 300 and 400°C (Passchier & Trouw 2005), and the phenoclasts record a top-to-the-SW sense of ductile shearing in the locally mylonitic zones (Figure 5f). In short, the increased intensity of solid-state fabrics is developed in the Dushan pluton from northeast to southwest (Figure 5g), without sharp boundaries between fabric types. In the southernmost part of the pluton, mylonitic fabrics are exposed in rocks close to the contact with host rocks.

5 RADIOMETRIC AGE DATA

Several radiogenic isotope age data have been documented in the Dushan pluton and its neighboring Dashizhu pluton (Figure 2). Late Triassic ages estimates using U-Pb zircon dating are consistent for the Dushan pluton (ranging from 223–215 Ma; Luo et al. 2003; Ye et al. 2014; Xu et al. 2016; Jiang et al. 2018), and they are similar to those of the Dashizhu pluton ranging from 266 to 224 Ma (Ye et al. 2014; Xiong et al. 2017). To clarify temporal relationship between two plutons, new high-precision U-Pb zircon dating was carried out using a Cameca IMS 1280 large-radius SIMS at Institute of Geology and Geophysics, Chinese Academy of Sciences (IGGCAS). Samples 17DS39 and DS44 are collected from the granodiorite in the southern Dashizhu pluton and the monzogranite in the western Dushan pluton, respectively (Figure 2).

The zircons extracted from these two samples are subhedral, transparent, and about 50–150 μm long. They have aspect ratios between 1:1 and 3:1. Euhedral oscillatory zoning is common in CL images (Figure 6a). Zircons from sample 17DS39 yield Th/U ratios between 0.14 and 1.21. The $^{206}Pb/^{238}U$ and $^{207}Pb/^{235}U$ results from twenty-one analyses are relatively consistent on a

Concordia diagram. An estimated Concordia value of 217.6±1.5 Ma supports an emplacement age of the Dushan pluton (Figure 6b and Table 1). Twenty-one analyses of sample DS44 were obtained, with the Th/U ratios ranging from 0.71 to 1.66. All analyses, excluding one inherited grain at 2437 Ma, yield a Concordia age of 225.6±1.5 Ma (Figure 6b and Table 1), implying a Late Triassic crystallization age of the Dashizhu pluton.

6 ANISOTROPY OF MAGNETIC SUSCEPTIBILITY (AMS) DATA

Macroscopic planar fabrics are lacking in the northeast and central parts of the Dushan pluton. Mineral lineations are absent when a planar fabric can be observed, except within mylonites. The relationships between magnetic fabrics and fabric elements of anisotropic rocks have been well established where macro and microscopic features cannot be observed (Archanjo et al. 1994; Bouchez & Gleizes 1995; Bouchez et al. 1997; Benn et al. 2001). Our AMS study on the Dushan pluton was intended to reveal its magnetic fabrics and define the surface structure of the pluton. An AMS study has not been performed on the adjacent Dashizhu pluton due to the poor exposures.

6.1. Sampling and Measurements

A total of 252 independent core samples from 41 sampling sites was collected in the Dushan pluton. At each site, five to eight sample cores of 2.5 cm in diameter have been obtained. These sample cores were cut into cylindrical specimens of 2.2 cm long in the laboratory. Both the anisotropy magnetic susceptibility and the bulk susceptibility were measured using a KLY4 susceptometer (Figure 7). The ANISOFT package was used for the statistical analysis of the AMS data (Jelinek 1981). The mean orientation of three principal axes of the AMS ellipsoid ($K_1 \geq K_2 \geq K_3$), the anisotropy degree (P_J), and the shape parameter (T) were calculated. In the

Laboratory of Paleomagnetism and Chronology of IGGCAS, Beijing, the magnetic mineralogy was investigated to identify the magnetic carriers by the following measurements (Figure 8), including acquisition of Isothermal Remanent Magnetization (IRM), thermomagnetic susceptibility curves, and hysteresis loops.

6.2. Magnetic Susceptibility Carriers

The mean magnetic susceptibility, $K_m = (K_1 + K_2 + K_3)/3$, of samples from 41 sampling sites shows a wide range of values in the Dushan pluton, from 397 to 25,800×10^{-6} SI (Figure 7a and Table 2). A total of 39 out of 41 AMS (more than 95%) sites reveal high K_m values (> 500×10^{-6} SI), indicating that ferrimagnetic minerals are the principal magnetic carriers (Figure 7a and Table 2; Bouchez 2000). Only two AMS sites (DS17 and DS20) display K_m values less than 500×10^{-6} SI, usually attributed to a dominant paramagnetic contribution. A broad correlation is present between K_m variations and petrographic facies type, i.e., lower K_m values for the biotite monzogranite marginal facies and higher ones for other facies (Figure 9a).

The hysteresis loops of six representative samples display nonlinear variations of hysteresis curves, indicative of the dominance of ferrimagnetic minerals (Figures 8a-8b). All IRM acquisition curves show a sudden saturation and concave downward curve below 300 mT (Figures 8c-8d). The thermomagnetic measurements mainly display rapid drops of magnetic susceptibility at 550-600°C, suggesting that magnetite is the principal susceptibility carrier(Figures 8e-8f). The sample DS39 shows a rapid rise at higher temperature during the cooling process probably due to mineral transformations during the heating process. The domain of most magnetite grains could mainly be pseudo-single domain (PSD) according to the ratios of Mr/Ms and Hcr/Hc (Dunlop 2002; Figure 7b).

In conclusion, despite the presence of abundant biotite in the Dushan pluton, magnetite is the principal magnetic contributor in more than 96% of AMS sites. For two sites (DS17 and DS20), biotite may be a significant magnetic susceptibility contributor. The magnetic susceptibility varies from petrofacies type and relative contents of magnetite. Moreover, the paramagnetic and ferrimagnetic minerals can often carry compatible magnetic fabrics (Archanjo et al. 1994; Martín-Hernández & Hirt 2003). Because the single-domain (SD) magnetite that could result in inverse fabrics is not present in a significant amount, the lineation and the normal to foliation could correspond to the K_1 and K_3 axes of the magnetic susceptibility ellipsoid, respectively (e.g., Hargraves et al. 1991; Tarling & Hrouda 1993).

6.3. Anisotropy Degree and Shape Parameter

More than 58% of the sampling sites in the Dushan pluton display an anisotropy degree higher than 1.2 with a positive correlation between P_J and K_m (Figure 7). In the arc-shaped gneissic and, locally, mylonitic zones where moderate to strong solid-state deformation occurred, the P_J values are not higher than the other sampling sites (Figure 9b). Therefore, we hypothesize that the higher P_J values do not correlate with strain intensity but with greater concentration amount of magnetite. The shape parameter T varies from -0.728 to +0.733 (Figures 7d-7e). The shape parameters with both negative and positive T values are mainly from the sites in the southwest part of the Dushan pluton that essentially belongs to the arc-shaped gneissic and, locally developed, mylonitic zone (Figure 9c). The anisotropy degree and the shape of the AMS ellipsoid are usually characterized by P_J and T parameters, respectively (Jelinek 1981). These parameters, based on the high variability, cannot be used to constrain strain patterns in this study.

6.4. AMS Fabric Pattern and Comparison with Rock Petro-fabric

For each site, K_1 and K_3 axes are characterized by site-average orientations of principal axes dispersion with a corresponding 95% confidence level (α_{95max} and α_{95min}) (Jelinek 1978; Figure 10). We consier the corresponding magnetic axis as well-defined if a confidence level is less than 25°. Otherwise, the magnetic axis is poorly defined. For both K_1 and K_3 axes, the former is the case for more than 74% of the AMS sites. In the arc-shaped gneissic monzogranite with locally mylonitic zones, the magnetic foliations are in agreement with the mesoscopic fabrics observed in the field (Figure 11).

In the Dushan pluton, both mesoscopic and magnetic foliations with moderate to steep outward dips define an elliptic pattern with a NE-SW long axis (Figure 11a). The foliations are sub-vertical in the northeast part of the pluton and dip inward and strike sub-parallel to the border of the pluton close to the southeastern border. The magnetic lineations display gently to moderate NE-SW plunges throughout the pluton except in its northeastern part where they become more scattered in trend and are locally steeply plunging (Figure 11b).

7 GRAVITY MODELING

Gravity modeling has been proven effective in describing the geometry of deep crustal structures, including granitic plutons (Vigneresse 1990; Améglio & Vigneresse 1999). In the Dushan pluton, a gravity modeling study was performed to better define its geometry, shape, and possible feeder zones. Meanwhile, the Dashizhu pluton has also been included in the survey, to clarify its relationship with the Dushan pluton in the gravity modeling study. The Bouguer anomaly map (1: 200,000), derived from the Chinese regional gravity survey, is available for gravity modeling. The short wavelengths of the gravity anomaly pattern are mainly derived from the surface down to a few kilometers. In order to highlight the Dushan pluton-related anomalies,

the long wavelengths of the complete Bouguer anomaly must be removed using a low-pass Butterworth filter from a lower-resolution (2′×2′) Bouguer grid (Bonvalot et al. 2012). The 380-km wavelength cutoff was considered as the best regional trend after several attempts. After subtracting the 380 km low-pass Butterwort filtered regional Bouguer anomaly, the residual Bouguer anomaly map was acquired (Figure 12a). The residual Bouguer anomaly map matches gravity anomalies and surface geological features well, suggesting that it is of good quality to characterize the geometry of the Dushan pluton.

Based on the residual Bouguer anomaly map, 2-D gravity modeling is also carried out to characterize the Dushan pluton at depth along four cross-sections, perpendicular to the long and short axes of the pluton (Figure 12b). Several factors, including structural data, lithologic units, geologic contacts, and density of lithologic units, have been taken into account in modeling. In our modeling, all available information from geologic maps and field observations have been taken into account, namely that Neoproterozoic carbonate rocks overlie Archaean gneiss, and that the granite was emplaced into the Malanyu anticline. Densities of these rock types have been determined by laboratory measurements (Lin et al. 2013) and are summarized in Figure 12b.

The negative gravity anomalies show a NE-SW trending elliptical shape that more or less correlates with the main geologic boundary of the Dushan pluton (Figure 12a). A negative anomaly is centered in the northeast part of the Dushan pluton and corresponds to the pluton root. To the north, the negative anomaly beyond the contact is likely due to an outward extension of the pluton below the country rocks. A maximum thickness (~7 km) of the pluton in the northeast progressively decreases southwestward to ~1 km. However, a high negative anomaly exists close to the southwestern border, implying local thickening of the pluton. The Dushan pluton shows a southwestward thinning tongue-like shape with a feeder zone in its northeast part.

In the Dashizhu pluton, the negative anomaly, located in the west part of the current exposure, is beyond the contact with cover rocks. The NE trending largest negative anomaly, which likely represents its root, is located in the western corner of the current exposure. The negative gravity anomaly changes into a positive anomaly away from the western corner. The Dashizhu pluton is interpreted as a funnel shape that sharply thins outward from a feeder zone in its western corner.

8 DISCUSSION

8.1. Fabric variation from magmatic to solid-state conditions in the Dushan pluton

The central and northeast parts of the Dushan pluton display weak or invisible mineral preferred orientation (Figures 4a-4b). However, a gneissic foliation, even with locally developed mylonitic structures, defines the SW pluton margin (Figures 2 and 4c-4f). No sharp boundaries between these magmatic and solid-state fabrics are observed (Figure 5). The strong solid-state fabrics are only distributed in the mylonitic zones in the southernmost part of the pluton (Figure 5g). The pervasive gneissic foliations develop in the southwest part, and the mylonitic fabric is only exposed near the margin. However, country rocks do not show a parallel penetrative fabric that appears to be restricted in the pluton. Strongly flattened xenoliths of the country rocks without any stretching lineation are distributed in the gneissic monzogranite (Figure 4d). The mylonitic zones have a top-to-the-SW ductile fabric (Figures 5f and 11b). These structural data suggest that the Dushan pluton underwent a southwestward increasing strain gradient in solid-state deformation.

Magmatic fabrics remain well-preserved in the northeast part of the Dushan pluton (Figure 5g). Moreover, the mesoscopic planar fabrics (i.e., gneissic and mylonitic foliations) are

geometrically compatible with the magnetic foliations that strike subparallel to the pluton border (Figure 11a). In map view, the elliptic dome-like pattern of the pluton, along with a NE-SW striking long axis, is consistent with both mesoscopic and magnetic foliations, despite the inward dips present near the southeast border of the pluton. The stretching lineations in the mylonitic zones trend NE-SW and are also concordant with magnetic lineations measured in the pluton (Figure 11b). Based on this dome-like geometry with the absence of top-to-the-SW ductile shearing in the country rocks, we argue for the contemporaneity between pluton emplacement and solid-state deformation. Our field and microscopic observations, together with AMS data, suggest a continuum of fabric variation from magmatic to solid-state conditions during emplacement of the Dushan pluton.

8.2. Fabric development mode

The Dashizhu pluton presents a funnel-shaped architecture with a feeder zone in the northwest corner of its exposure (Figures 12b and 13). The Dashizhu pluton sharply thins away from the feeder zone, implying that the current exposure may be also close to the root of the Dashizhu pluton. Based on the geochronologic data from both plutons (Figure 6), the Dashizhu pluton intruded into the Malanyu anticline at ca. 225 Ma, then the Dushan pluton intruded against the southwest sidewall of the Dashizhu pluton at ca. 217 Ma.

The Dushan pluton shows a southwestward thinning tongue-like shape with a feeder zone in its northeast part. The roof is estimated to have a dome-like structure due to the moderate to steep outward dipping foliations parallel to the margin (Figure 12a), with the exception of the biotite-rich marginal facies. Close to the southeast border, the foliations dip inwards and strike sub-parallel to the pluton border. These foliations roughly conform to the foliations of the host rocks near the pluton (Figure 2). The biotite-rich magma probably first ascended via the feeder

zone and was injected as a sill into the Malanyu anticline (Figure 13). The later monzogranite magma likely upwelled, inflated, and pushed aside the country rocks to build the Dushan pluton. No internal petrographic zoning within the pluton with sharp facies boundaries was found, although a progressive mineral fabric change is present. Because no similar penetrative fabrics parallel to these of the pluton were developed in the host rocks, it is likely that the emplacement of the Dushan pluton cannot be interpreted as a nested diapir of expanded plutons that implies the rising of large magma batches, but rather inflation of conduit-fed magma batches (Paterson & Vernon 1995).

Several lines of evidence suggest that magma inflation occurred not only upwards and downwards, but also laterally. These include the following features: (1) a dome-like roof marked by outward dipping foliations; (2) an irregular floor with inward dipping sidewalls; (3) strongly flattened xenoliths without stretching lineations in the gneissic monzogranite; (4) deflection of country-rock structures; and (5) an arc-shaped fold-and-thrust belt that wraps around the Dushan pluton in the northwest. The dominant NE-SW lineations may reflect southwest-directed intrusion, due possibly to the blocking of Dashizhu pluton magma to the northeast (Figure 11b). The magma spread southwestward from the feeder zone until the loss of heat and its crystallization, while the younger magma continued to expand the already crystallized southwest margin. Magma inflation resulted in an arc-shaped, gneissic to mylonitic foliation along the southwest margin by subsolidus deformation (Figure 13). The flattened xenoliths are aligned parallel to magmatic foliations along the southwest margin, forming strain indicators of the expansion event (Figure 4d). The dome-like roof with outward dipping foliations was exhumated, leaving preserved biotite-rich marginal facies (Figure 13). In the biotite-rich marginal facies, the foliations retain original inward dips in the southeast but have outward dips

elsewhere due to the pluton inflation (Figure 11b). Fabric development seems to have occurred in a relatively continuous process during pluton emplacement, resulting in no sharp contact between the rocks with magmatic and solid-state fabrics. The subsequent solid-state overprint mainly occurred along the southwest margin, mainly leaving preserved magmatic fabrics in the northeast.

In brief, the formation of the Dushan pluton probably began with the ascent of a sill-like body then evolved into inflation by magma batches. This main southwestward-directed intrusion deformed the former cool-down magma, forming a curved gneissic to mylonitic foliation in its southwest margin. A continuum of magma chamber-related fabrics from magmatic to solid-state conditions occurred within the pluton during pluton emplacement.

8.3. Tectonic implications

The fabrics exposed in the Dushan pluton may, in principle, be explained by a combination of magma intrusion, pluton inflation, and/or syn-emplacement solid-state deformation. Evidence for syn-magmatic ductile shearing coeval with the fabrics is observed within the Dushan pluton, but these fabrics are absent in the country rocks. Moreover, no syn-emplacement penetrative solid-state fabrics parallel to the fabrics in the pluton are present in the country rocks. Therefore, we hypothesize that pluton emplacement was probably driven by magma buoyancy without a significant influence of regional tectonics. In other words, both mesoscopic and magnetic fabrics in the Dushan pluton were related to the magmatic construction process rather than to the Late Triassic regional extension in the northern NCC. Our study implies that, despite emplacement in a specific tectonic setting, nearly contemporaneous plutons may contain within them a diversity of fabric characteristics, including solid-state mylonitic fabrics, that are the result of emplacement. We argue that not all fabrics within plutons associated with a specific tectonic

setting should be used to provide information on regional tectonics. Instead, the fabric patterns in both pluton and host rock need to be carefully documented and magmatic emplacement origins ruled out based on geometric and fabric distribution arguments. Both magmatic and solid-state fabrics within plutons need to be examined carefully to infer regional tectonics.

9 CONCLUSIONS

Based on a multidisciplinary approach, we propose the development model of a continuum of magma chamber-related magmatic to solid-state fabrics for the Dushan pluton during its emplacement at ca. 217 Ma. The tongue-like Dushan pluton was probably constructed through its northeastern feeder zone, with an early biotite-rich sill-shape intrusion followed by inflation by conduit-fed monzogranite magma batches. Inflation occurred during the progressive and southwestward-directed magma intrusions. This inflation deformed the early cooled-down magma that we infer to have been sufficiently crystallized to deform by solid-state processes. This deformation leads to an arc-shaped, gneissic to mylonitic foliation in its southwest margin, leaving preserved magmatic fabrics in the northeast. Although fabrics in plutons, especially late-stage solid-state fabrics, may record evidence of regional tectonics, it seems not the case of this study, i.e., the fabrics did probably not reflect regional tectonics. Such fabrics within plutons need to be used with caution for inferring regional tectonics.

ACKNOWLEDGMENTS

This study received financial support from the National Key R&D Program of China (2016YFC0600102) and the National Natural Science Foundation of China (91855212 and 91755205). We also appreciate the support from LABEX VOLTAIRE (ANR-10-LABX-100-01), and EQUIPEX PLANEX (ANR-11-EQPX-0036). Profs. John Geissman and Silvana Geuna

together with the editors Eduard Petrovsky and Fern Storey are very much thanked for their constructive comments and carefull editing. Great thanks are also due to Profs. Jiří Žák and Jean-Luc Bouchez for their constructive suggestions.

DATA AVAILABILITY

The field, radiogenic age, and AMS data underlying this paper are available in the figures, tables, and cited references. The gravity data used for this study is provided by China Geological Survery (CGS). We only have the right to use it, cannot share it with others. If the reader is interested in the data, he/she can contact CGS (nga@mail.cgs.gov.cn) for permission.

REFERENCES

Améglio, L. & Vigneresse, J. L., 1999. Geophysical imaging of the shape of granitic intrusions at depth: a review. Geological Society, London, Special Publications, 168 (1), 39–54. https://doi.org/10.1144/GSL.SP.1999.168.01.04

Archanjo, C. J., Launeau, P. & Bouchez, J. L., 1994. Magnetic fabrics vs. magnetite and biotite shape fabrics of the magnetite-bearing granite pluton of Gameleiras (Northeast Brazil), Physics of the Earth and Planetary Interiors, 89 (1–2), 63–75. https://doi.org/10.1016/0031-9201(94)02997-P

Archanjo, C.J., Trindade, R.I.F., Bouchez, J.L. & Ernesto, M., 2002. Granite fabrics and regional-scale strain partitioning in the Seridó belt (Borborema province, NE Brazil), Tectonics, 21 (1), 3-1–3-14.

Barboni, M., Schoene, B., Ovtcharova, M., Bussy, F., Schaltegger, U. & Gerdes, A., 2013. Timing of incremental pluton construction and magmatic activity in a back-arc setting revealed

by ID-TIMS U/Pb and Hf isotopes on complex zircon grains, Chemical Geology, 342, 76-93. https://doi.org/10.1016/j.chemgeo.2012.12.011

Benn, K., Paterson, S.R., Lund, S.P., Pignotta, G.S. & Kruse, S., 2001. Magmatic fabrics in plutons as markers of regional strains and plate kinematics: Example of the Cretaceous Mt. Stuart pluton, Physics and Chemistry of the Earth Part A Solid Earth and Geodesy, 26 (4–5), 343–354. https://doi.org/10.1016/S1464-1895(01) 00064-3

Blumenfeld, P. & Bouchez, J.L., 1988. Shear criteria in granite and migmatite deformed in the magmatic and solid states, Journal of Structural Geology, 10, 361-372.

Bonvalot, S., Balmino, G., Briais, A., Kuhn, M., Peyrefitte, A., Vales, N. & Biancale, R., et al., 2012. World gravity map. (1:50000000 map), BGI-CGMWCNES-IRD, Paris.

Bouchez, J.L., 2000. Anisotropie de susceptibilité magnétique et fabrique des granites (Magnetic susceptibility anisotropy and fabrics in granites), Comptes Rendus de l'Académie des Sciences Paris, 330, 1–14.

Bouchez, J.L. & Gleizes, G., 1995. Two-stage deformation of the Mount-Louis-Andorra granite pluton (Variscan Pyrenees) inferred from magnetic susceptibility anisotropy, Journal of the Geological Society, 152 (4), 669–679. https://doi.org/10.1144/gsjgs.152.4.0669

Bouchez, J.L., Hutton, D. & Stephens, W.E., 1997. Granite is Never Isotropic: An Introduction to AMS Studies of Granitic Rocks. Granite: From Segregation of Melt to Emplacement Fabrics (pp. 95–112). Paris: Springer Science & Business Media. https://doi.org/10.1007/978-94-017-1717-5_6

Davis, G.A., Meng, J.F. & Cao, W.R., 2009. Triassic and Jurassic tectonics in the eastern Yanshan belt, North China: insights from the controversial Dengzhangzi Formation and its

neighboring units, Earth Science Frontiers, 16 (3), 69–86. https://doi.org/10.1016/S1872-5791(08)60090-1

Davis, G.A., Xu, B., Zheng, Y.D. & Zhang, W.J., 2004. Indosinian extension in the Solonker suture zone: the Sonid Zuoqi metamorphiccore complex, Inner Mongolia, China, Earth Science Frontiers, 11 (3), 135–144. https://doi.org/ 10.1007/BF02873097

Davis, G.A., Zheng, Y.D. & Wang, C., 2001. Mesozoic tectonic evolution of the Yanshan Fold-and-Thrust Belt, with emphasis on Hebei and Liaoning provinces, northern China. In: Hendrix, M.S., Davis, G.A. (Eds.), Paleozoic and Mesozoic tectonic evolution of central Asia: From continental assembly to intracontinental deformation, Boulder, Colorado, Geological Society of America Memoir, 194, 171–197.

De Saint Blanquat, M., Horsman, E., Habert, G., Morgan, S., Vanderhaeghe, O., Law, R. & Tikoff, B., 2011. Multiscale magmatic cyclicity, duration of pluton construction, and the paradoxical relationship between tectonism and plutonism in continental arcs, Tectonophysics, 500 (1–4), 20–33. https://doi.org/10.1016/j.tecto.2009.12.009

Dunlop, D.J., 2002. Theory and application of the day plot (Mrs/Ms versus Hcr/Hc) 1. Theoretical curves and tests using titanomagnetite data, Journal of Geophysical Research, 107 (B3), 2056. https://doi.org/10.1029/2001JB000487

Faure, M. & Pons, J., 1991. Crustal thinning recorded by the shape of the Namurian–Westphalian leucogranite in the Variscan belt of the Northwest Massif Central, France, Geology, 19, 730–733.

Faure, M., Lin, W. & Chen, Y., 2012. Is the Jurassic (Yanshanian) intraplate tectonics of North China due to westward indentation of the North China block? Terra Nova, 24 (6), 456–466. https://doi.org/10.1111/ter.12002

Gleizes, G., Leblanc, D. & Bouchez, J.L., 1997. Variscan granites of the Pyrenees revisited: their role as syntectonic markers of the orogen, Terra Nova, 9, 38–41.

Hargraves, R.B., Johnson, D. & Chan, C.Y., 1991. Distribution anisotropy: the cause of AMS in igneous rocks? Geophysical Research Letters, 18 (12), 2193–2196. https://doi.org/10.1029/91GL01777

Hutton, D.H.W., 1988. Granite emplacement mechanisms and tectonic controls: inferences from deformation studies, Earth and Environmental Science Transactions of the Royal Society of Edinburgh, 79, 245–255.

Jelinek, V., 1978. Statistical processing of anisotropy of magnetic susceptibility measured on groups of specimens, Studia Geophysica et Geodaetica, 22 (1), 50–62. https://doi.org/10.1007/BF01613632

Jelinek, V., 1981. Characterization of the magnetic fabric of rocks, Tectonophysics, 79 (3–4), T63–T67. https://doi.org/10.1016/0040-1951(81)90110-4

Jiang, S.H., Bagas, L., Liu, Y.F. & Zhang, L.L., 2018. Geochronology and petrogenesis of the granites in Malanyu anticline in eastern North China Block, Lithos, 312, 21–37. https://doi.org/10.1016/j.lithos.2018.04.028

Joly, A., Faure, M., Martelet, G. & Chen, Y., 2009. Gravity inversion, AMS and geochronological investigations of syntectonic granitic plutons in the southern part of the

Variscan French Massif Central, Journal of Structural Geology, 31 (4), 421–443. https://doi.org/10.1016/j.jsg.2009.01.004

Li, C., Zhang, C., Cope, T. D. & Lin, Y., 2016. Out-of-sequence thrusting in polycyclic thrust belts: an example from the Mesozoic Yanshan belt, North China Craton, Tectonics, 35, 2082–2116. https://doi.org/10.1002/2016TC004187

Lin, W., Charles, N., Chen, K., Chen, Y., Faure, M., Wu, L. & Wang, F., 2013. Late Mesozoic compressional to extensional tectonics in theYiwulüshan massif, NE China and its bearing on the evolution of the Yinshan–Yanshan orogenic belt part II: Anisotropy of magnetic susceptibility and gravity modeling, Gondwana Research, 23 (1), 78–94. https://doi.org/10.1016/j.gr.2012.02.012

Lin, W. & Wei, W., 2018. Late Mesozoic extensional tectonics in the North China Craton and its adjacent regions: A review and synthesis, International Geology Review, https://doi.org/10.1080/00206814.2018.1477073

Luo, Z.K., Miao, L.C., Guan, K., Qiu, Y.S., Qiu, Y.M., Mcnaughton, N.J. & Groves, D. I., 2003. SHRIMP U-Pb zircon dating of the Dushan granitic pluton and related granite-porphyry dyke, eastern Hebei province, China, and their geological significance (in Chinese with English abstract), Geochimica, 32 (2), 173–180.

Machek, M., Závada, P., Roxerová, Z., Petrovský, E., Špičák, A., & Kusbach, V., 2019. Crystal mush flow in small concentrically expanded pluton (Castle Crags Pluton; Klamath Mountains, CA, USA), Geochemistry, Geophysics, Geosystems, 20, 1954–1974. https://doi.org/10.1029/2018GC008018

Mahon, K.I., Harrison, T.M. & Drew, D.A., 1988. Ascent of a granitoid diapir in a temperature varying medium, Journal of Geophysical Research-Solid Earth and Planets, 93 (B2), 1174-1188. https://doi.org/10.1029/JB093iB02p01174

Martín-Hernández, F. & Hirt, A.M., 2003. Paramagnetic anisotropy of magnetic susceptibility in biotite, muscovite and chlorite single crystals, Tectonophysics, 367 (1–2), 13–28. https://doi.org/10.1016/S0040-1951(03)00127-6

Meng, Q.R., Wei, H.H., Wu, G.L. & Duan, L., 2014. Early Mesozoic tectonic settings of the northern North China Craton, Tectonophysics, 611 (1), 155–166. https://doi.org/10.1016/j.tecto.2013.11.015

Meng, Q.-R., Wu, G.-L., Fan, L.-G., Wei, H.-H. & Wang, E., 2020. Late Triassic uplift, magmatism and extension of the northern North China block: Mantle signatures in the surface, Earth and Planetary Science Letters, 547, 116451. https://doi.org/10.1016/j.epsl.2020.116451

Passchier, C.W. & Trouw, R. A. J., 2005. Microtectonics. Berlin-Heidelberg-New York: Springer.

Paterson, S.R., Fowler, T.K., Schmidt, K.L., Yoshinobu, A.S., Yuan, E.S. & Miller, R.B., 1998. Interpreting magmatic fabric patterns in plutons, Lithos, 44 (1-2), 53-82. https://doi.org/10.1016/s0024-4937(98)00022-x

Paterson, S.R. & Tobisch, O.T., 1992. Rates of processes in magmatic arcs: implications for the timing and nature of pluton emplacement and wall rock deformation, Journal of Structural Geology, 14, 291-300.

Paterson, S.R. & Vernon, R.H., 1995. Bursting the bubble of ballooning plutons: A return to nested diapirs emplaced by multiple processes, Geological Society of America Bulletin, 107 (11), 1356–1380. https://doi.org/10.1130/0016-7606(1995)107<1356:BTBOBP>2.3.CO;2

Paterson, S.R., Vernon, R.H. & Tobisch, O.T., 1989. A review of criteria for the identification of magmatic and tectonic foliations in granitoids, Journal of Structural Geology, 11 (3), 349–363.

Qiu, H., Lin, W., Faure, M., Chen, Y., Meng, L., Zeng, J., Reng, Z. Wang, Y. & Li, Q., 2020. Late Triassic extensional tectonics in the northern North China Craton, insights from a multidisciplinary study of the Wangtufang pluton, Journal of Asian Earth Sciences, 104462. https://doi.org/10.1016/j.jseaes.2020.104462

Stearns, M.A. & Bartley, J.M., 2014. Multistage emplacement of the McDoogle pluton, an early phase of the John Muir intrusive suite, Sierra Nevada, California, by magmatic crack-seal growth, Geological Society of America Bulletin, 126 (11-12), 1569-1579. https://doi.org/10.1130/B31062.1

Talbot, J.Y., Chen, Y. & Faure, M., 2005. A magnetic fabric study of the Aigoual–Saint Guiral–Liron granite pluton (French Massif Central) and relationships with its associated dikes, Journal of Geophysical Research: Solid Earth，110 (B12).

Talbot, J.Y., Chen, Y., Faure, M. & Lin, W., 2000. AMS study of the Pont-de-Montvert-Borne porphyritic granite pluton (French Massif Central) and its tectonic implications, Geophysical Journal International, 140 (3), 677–686. https://doi.org/10.1046/j.1365-246x.2000.00067.x

Talbot, J.Y., Martelet, G., Courrioux, G., Chen, Y. & Faure, M., 2004. Emplacement in an extensional setting of the Mont Lozère–Borne granitic complex (SE France) inferred from

comprehensive AMS, structural and gravity studies, Journal of Structural Geology, 26 (1), 11–28. https://doi.org/10.1016/S0191-8141(03)00083-X

Tarling, D.H. & Hrouda, F., 1993. Magnetic Anisotropy of Rocks. London, U.K., Chapman and Hall.

Turrillot, P., Faure, M., Martelet, G., Chen, Y. & Augier, R., 2011. Pluton-dyke relationships in a Variscan granitic complex from AMS and gravity modeling. Inception of the extensional tectonics in the South Armorican Domain (France), Journal of Structural Geology, 33 (11), 1681–1698. https://doi.org/10.1016/j.jsg.2011.08.004

Wang, Y., Zhou, L. & Zhao, L., 2013. Cratonic reactivation and orogeny: an example from the northern margin of the North China Craton, Gondwana Research, 24 (3-4), 1203–1222. https://doi.org/10.1016/j.gr.2013.02.011

Vigneresse, J.L., 1990. Use and misuse of geophysical data to determine the shape at depth of granitic intrusions, Geological Journal, 25 (3–4), 249–260. https://doi.org/10.1002/gj.3350250308

Xiao, W.J., Windley, B., Hao, J. & Zhai, M.G., 2003. Accretion leading to collision and the Permian Solonker suture, Inner Mongolia, China: termination of the Central Asian Orogenic Belt, Tectonics, 22, 1069–1089. http://doi.org/10.1029/ 2002TC001484.

Xiong, L., Wei, J., Shi, W., Fu, L., Li, H., Zhou, H. & Chen, M., 2017. Geochronology, petrology and geochemistry of the Mesozoic Dashizhu granites and lamprophyre dykes in eastern Hebei – western Liaoning: implications for lithospheric evolution beneath the North China Craton, Geological Magazine., 1–24. https://doi.org/ 10.1017/S0016756817000437

Xu, X., Jiang, N., Fan, W., Hu, J. & Zong, K., 2016. Petrogenesis and geological implications for the Mesozoic granites in Qinglong area, eastern Hebei Province (in Chinese with English abstract). Acta Petrologica Sinica, 32(1), 212–232.

Yang, J.H., Sun, J.F., Zhang, M., Wu, F.Y. & Wilde, S.A., 2012. Petrogenesis of silica-saturated and silica-undersaturated syenites in the northern North China Craton related to post-collisional and intraplate extension, Chemical Geology, 328 (11), 149–167. https://doi.org/10.1016/j.chemgeo.2011.09.011

Ye, H., Zhang, S.H., Zhao, Y. & Wu, F., 2014. Petrogenesis and emplacement deformation of the Late Triassic Dushan composite pluton in the Yanshan Fold-and-Thrust Belt: Implications for the tectonic settings of the northern margin of the North China Craton during the Early Mesozoic (in Chinese with English abstract), Earth Science frontiers, 21 (4), 275–292.

Žák, J., Kratinová, Z., Trubač, J., Janoušek, V., Sláma, J. & Mrlina, J., 2011. Structure, emplacement, and tectonic setting of Late Devonian granitoid plutons in the Teplá–Barrandian unit, Bohemian Massif, International Journal of Earth Sciences, 100 (7), 1477–1495. https://doi.org/10.1007/s00531-010-0565-7

Žák, J., Verner, K., Holub, F. V., Kabele, P., Chlupáčová, M. & Halodová, P., 2012. Magmatic to solid state fabrics in syntectonic granitoids recording early Carboniferous orogenic collapse in the Bohemian Massif, Journal of Structural Geology, 36, 27–42. https://doi.org/10.1016/j.jsg.2011.12.011

Žák, J., Verner, K. & Tycova, P., 2008. Multiple magmatic fabrics in plutons: an overlooked tool for exploring interactions between magmatic processes and regional deformation? Geological Magazine, 145 (4), 537–551. https://doi.org/10.1017/S0016756808004573

Zhang, S.H., Zhao, Y., Ye, H., Hou, K.J. & Li, C.F., 2012. Early Mesozoic alkaline complexes in the northern North China Craton: implications for cratonic lithospheric destruction, Lithos, 155, 1–18. https://doi.org/10.1016/j.lithos.2012.08.009

Zhang, S.H., Zhao, Y., Davis, G.A., Ye, H. & Wu, F., 2014. Temporal and spatial variations of Mesozoic magmatism and deformation in the North China Craton: implications for lithospheric thinning and decratonization, Earth-Science Reviews, 131 (4), 49–87. https://doi.org/10.1016/j.earscirev.2013.12.004

Zhao, G., Wilde, S.A., Cawood, P.A. & Sun, M., 2001. Archean blocks and their boundaries in the North China Craton: lithological, geochemical, structural and P-T, path constraints and tectonic evolution, Precambrian Research, 107 (1), 45–73. https://doi.org/10.1016/S0301-9268(00)00154-6

Zibra, I., Kruhl, J.H., Montanini, A. & Tribuzio, R., 2012. Shearing of magma along a high-grade shear zone: evolution of microstructures during the transition from magmatic to solid-state flow, Journal of Structural Geology, 37(4), 150-160.

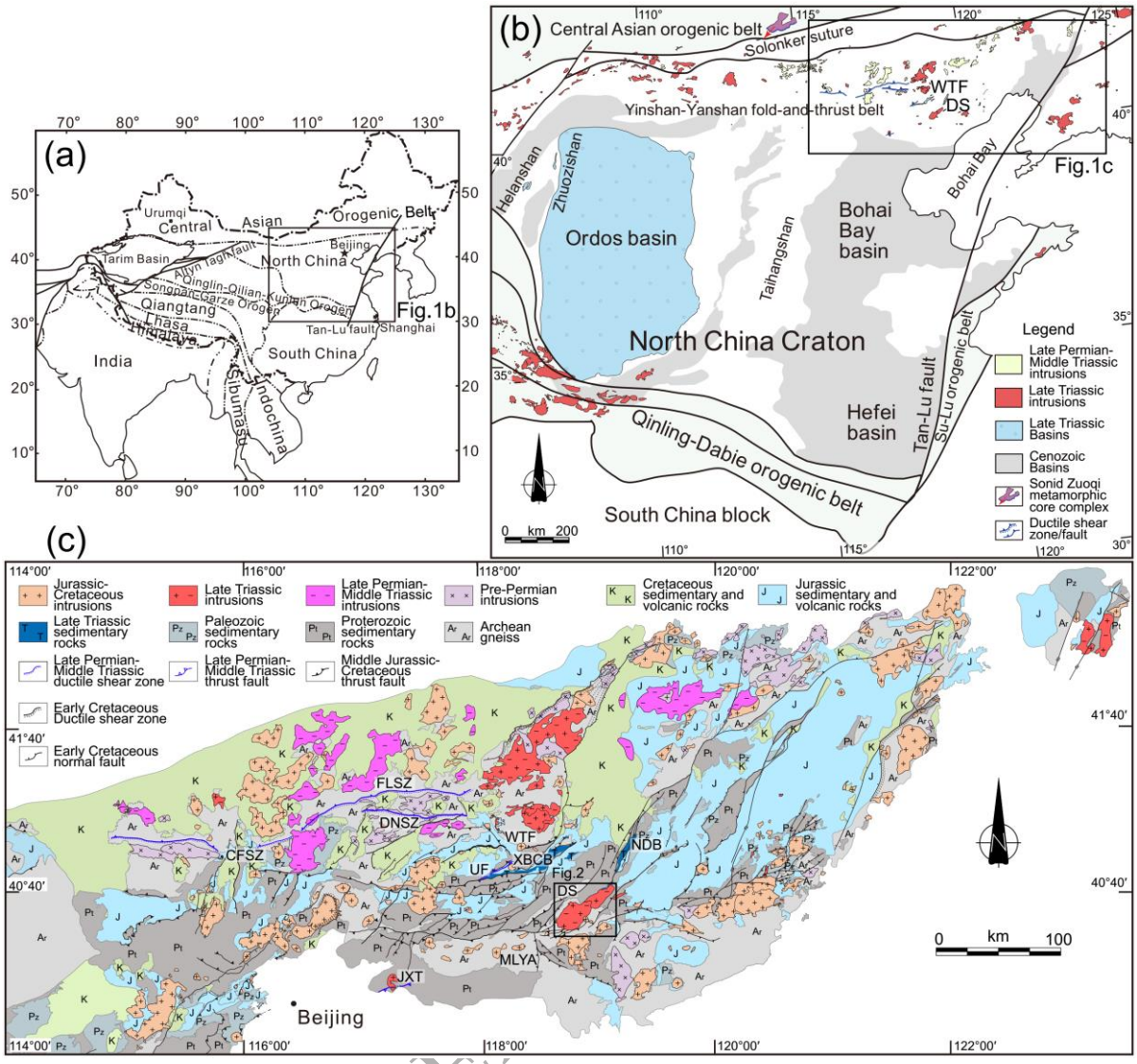

Figure 1. Overview maps of the Dushan pluton and its surrounding area (modified from Qiu et al. 2020). (a) Simplified tectonic map of China. (b) Triassic tectonic framework of the NCC. (c) Simplified tectonic map of the Yanshan fold-and-thrust belt. CFSZ: Chicheng-Fengning ductile shear zone, FLSZ: Fengning-Longhua, ductile shear zone, DNSZ: Damiao-Niangniangmiao ductile shear zone, UF: Unnamed fault, JXT: Jixian thrust, MLYA: Malanyu anticline, XBCB: Xiabancheng basin, YZB: Yingzi basin, NDB: Niuying-Dengzhangzi basin, DS: Dushan pluton; WTF: Wangtufang pluton.

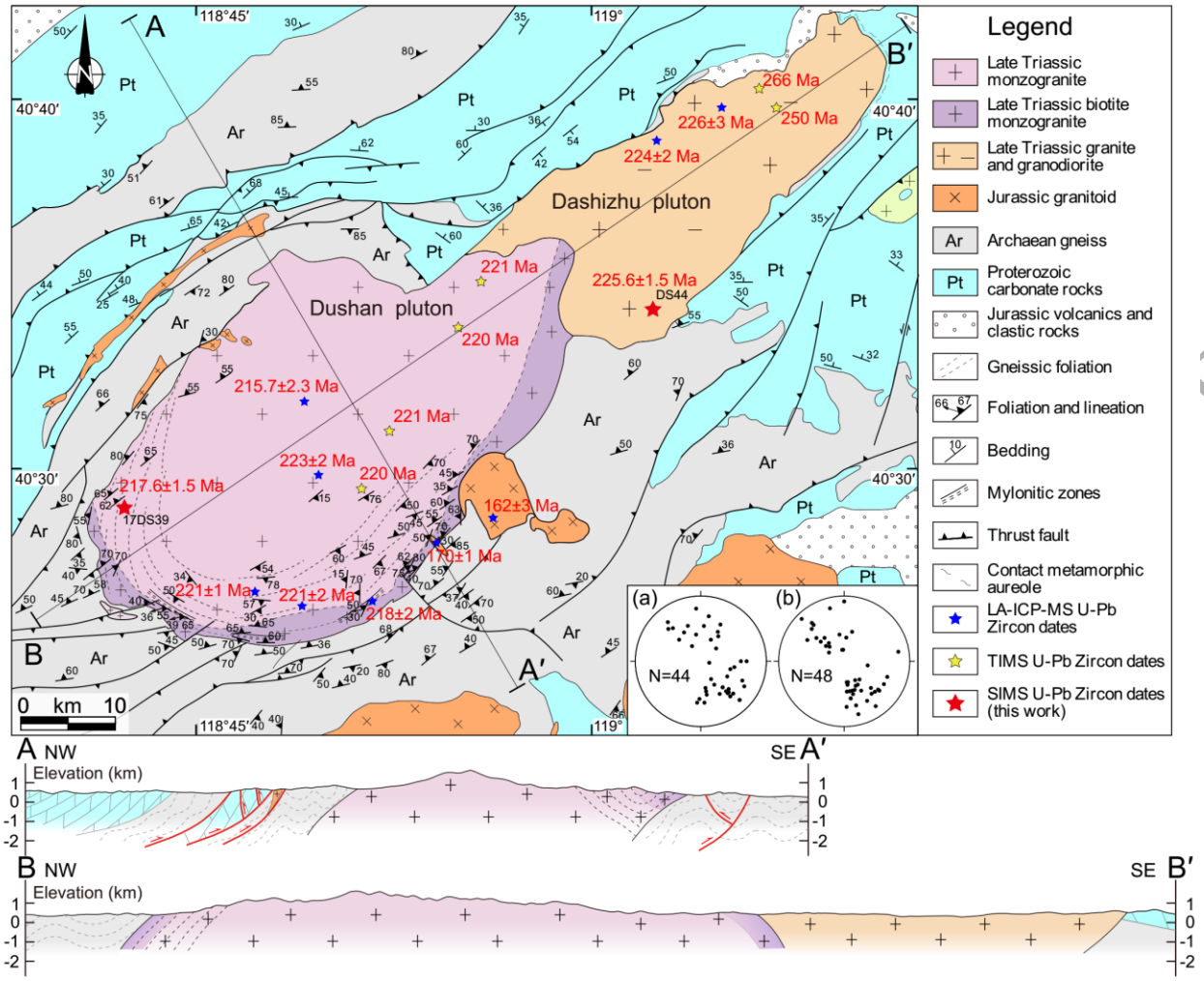

Figure 2. Structural map of the Dushan pluton and adjacent area. U–Pb zircon data from: Jiang et al. (2018); Luo et al. (2003); Xu et al. (2016); Ye et al. (2014); Xiong et al. (2017). (a) Stereonet for foliations in the Dushan pluton; (b) Stereonet for foliations in the country rocks.

Figure 3. Field photographs of the country rocks. (a) Western contact between the Dushan pluton and its country rocks. (b) Country rocks in the southeast of the Dushan pluton. (c) Folded gneiss to the south of the Dushan pluton. (d) Country rocks in the north of the Dushan pluton.

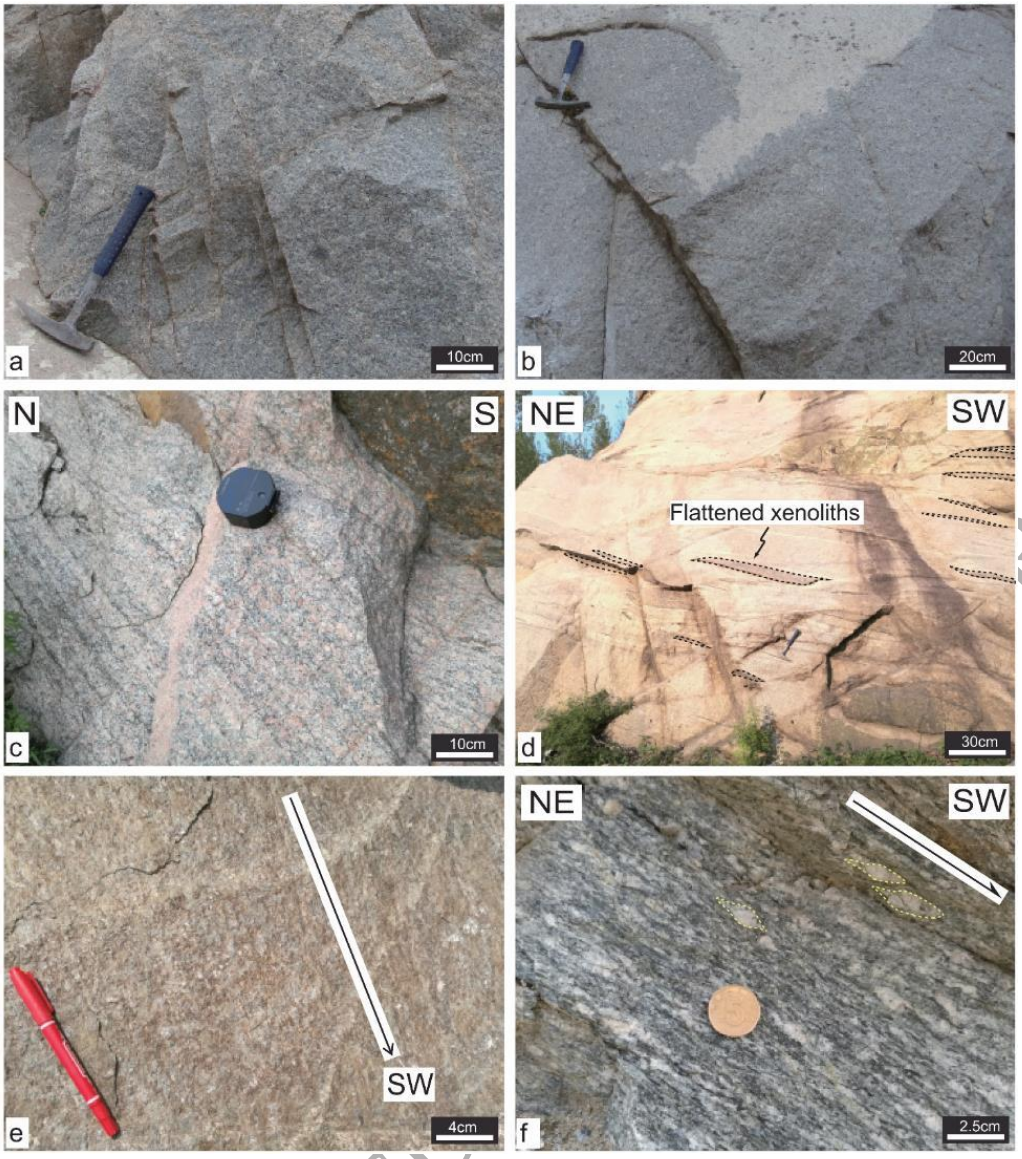

Figure 4. Field observations of the Dushan pluton. (a) Isotropic monzogranite in the northeastern part of the Dushan pluton. (b) Isotropic monzogranite in the central part of the Dushan pluton. (c) Foliation defined by biotite flakes and K-feldspars (southwest of the Dushan pluton). (d) Flattened xenoliths (southwest of the Dushan pluton). (e) NE-SW trending mineral lineations in mylonitic monzogranite of the Dushan pluton. (f) Sigmoidal feldspar porphyroclasts in mylonitic monzogranite in the Dushan pluton, showing a top-to-the-SW shearing (the section is parallel to lineation and perpendicular to foliation).

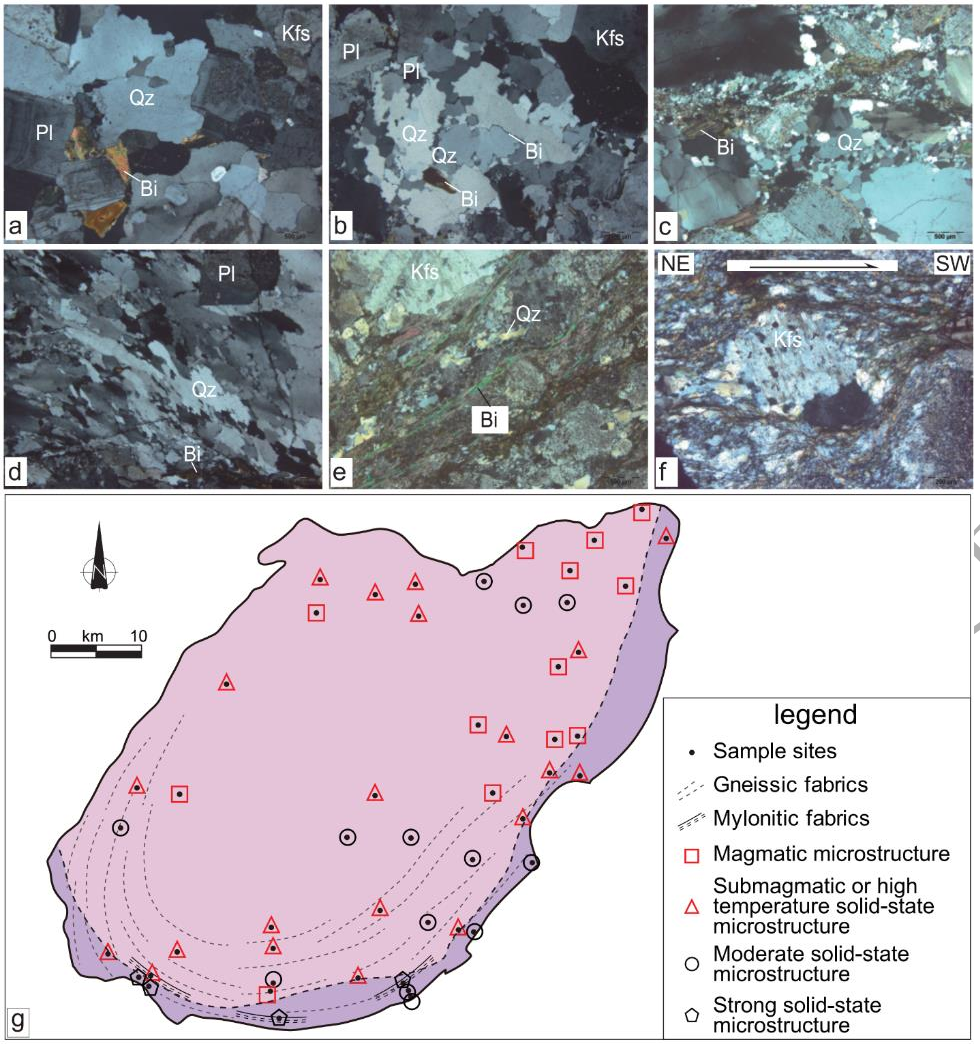

Figure 5. Microstructures of typical investigated samples in the Dushan pluton. (a) Magmatic microstructures in the northeastern part of the Dushan pluton. (b) Submagmatic or high temperature solid-state microstructures in the northern Dushan pluton. (c) Moderate solid-state microstructures in the central Dushan pluton. (d) Moderate solid-state microstructures in the southern Dushan pluton. (e) Strong solid-state microstructures in the southern Dushan pluton. (f) Strong solid-state microstructures in mylonitic monzogranite of the Dushan pluton. (g) Distribution map of the different types of microstructures. Bi = biotite, Kfs = K-feldspar, Pl = Plagioclase, Qz = quartz.

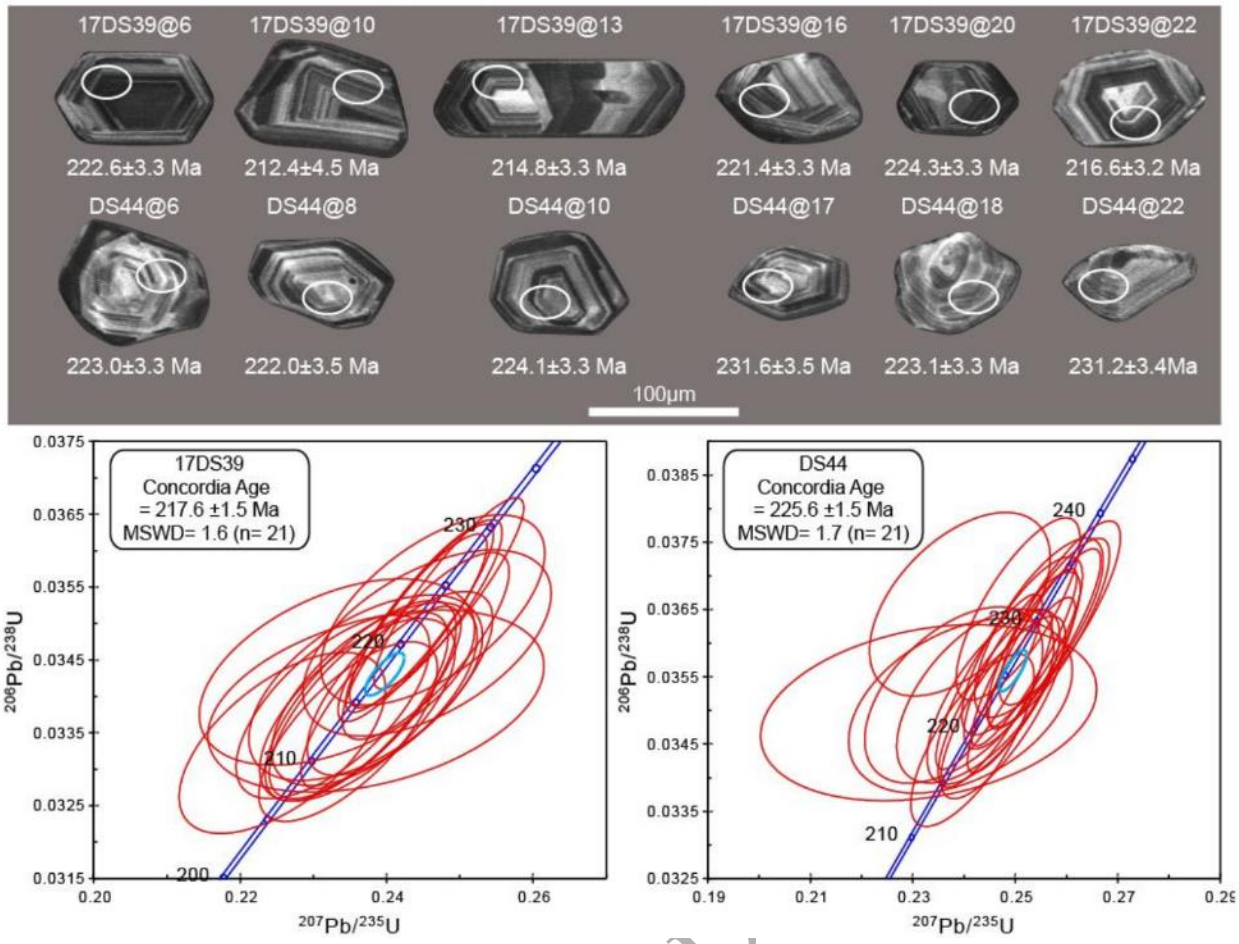

Figure 6. Cathodoluminescence (CL) images and U-Pb diagrams of Concordia age of representative zircons from collected samples. White elliptical circles are Secondary Ion Mass Spectrometer (SIMS) analysis locations; the numbers are ages. MSWD: mean square of weighted deviates.

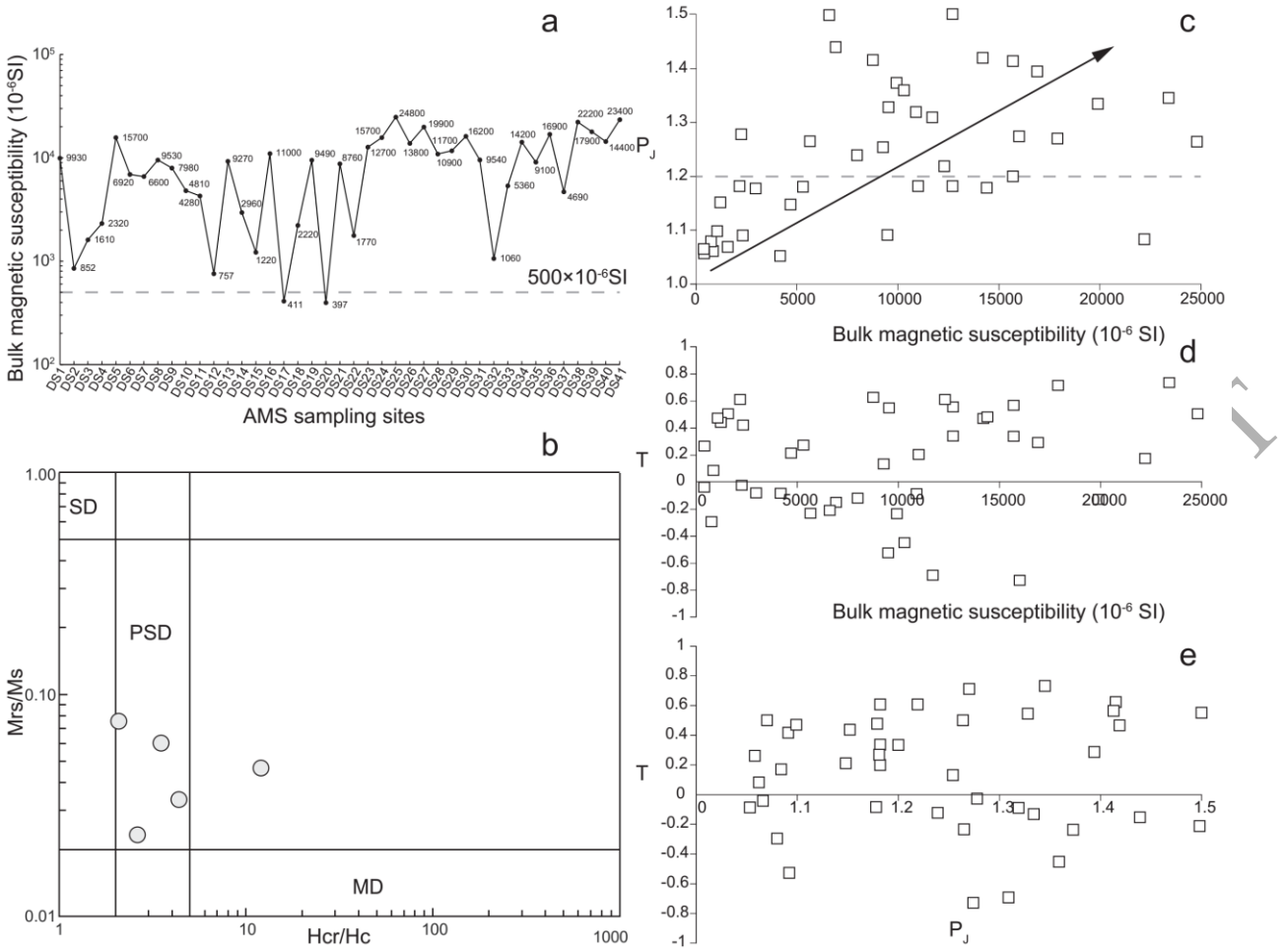

Figure 7. AMS scalar parameters of the Dushan pluton. (a) Site mean magnetic susceptibility (K_m). (b) Day plot of hysteresis parameters. Mrs: saturation of magnetic remanence, Ms: saturation of induced magnetization, Hcr: coercivity of magnetic remanence, Hc: coercivity of the measured sample. SD: single domain, PSD: pseudo-single domain, MD: multiple domain. (c) Bulk magnetic susceptibility K_m versus anisotropy degree P_J value. (d) Bulk magnetic susceptibility K_m versus shape parameter T. (e) Anisotropy degree P_J value versus shape parameter T.

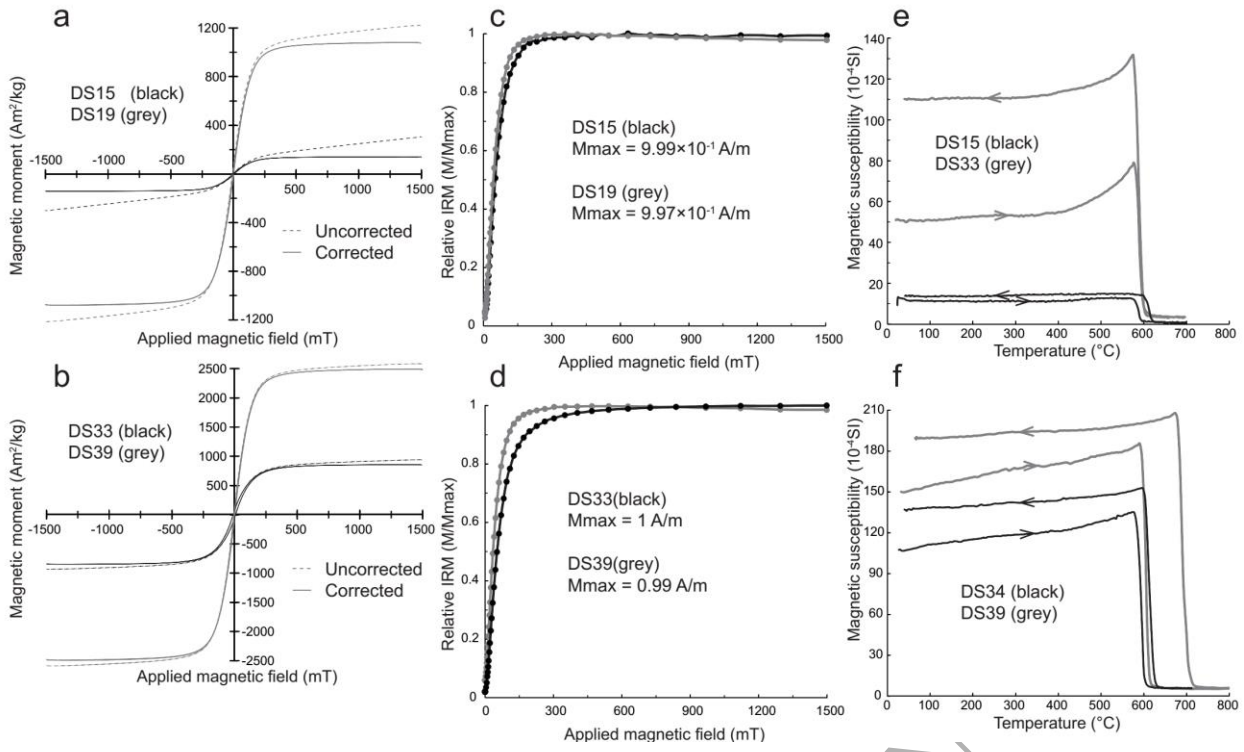

Figure 8. Magnetic mineralogy investigations of representative specimens from the Dushan pluton. (a–b) hysteresis loops, (c–d) acquisition of isothermal remanent magnetization (IRM), and (e–f) thermomagnetic curves (K (T) curves).

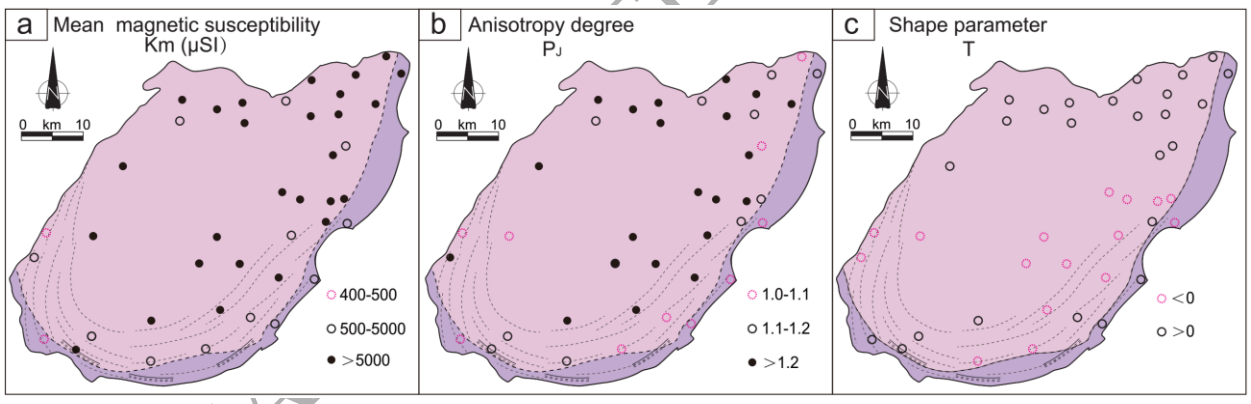

Figure 9. AMS maps of the Dushan pluton (a) Mean magnetic susceptibility map; (b) Anisotropy degree map; and (c) Shape parameter map in the Dushan pluton.

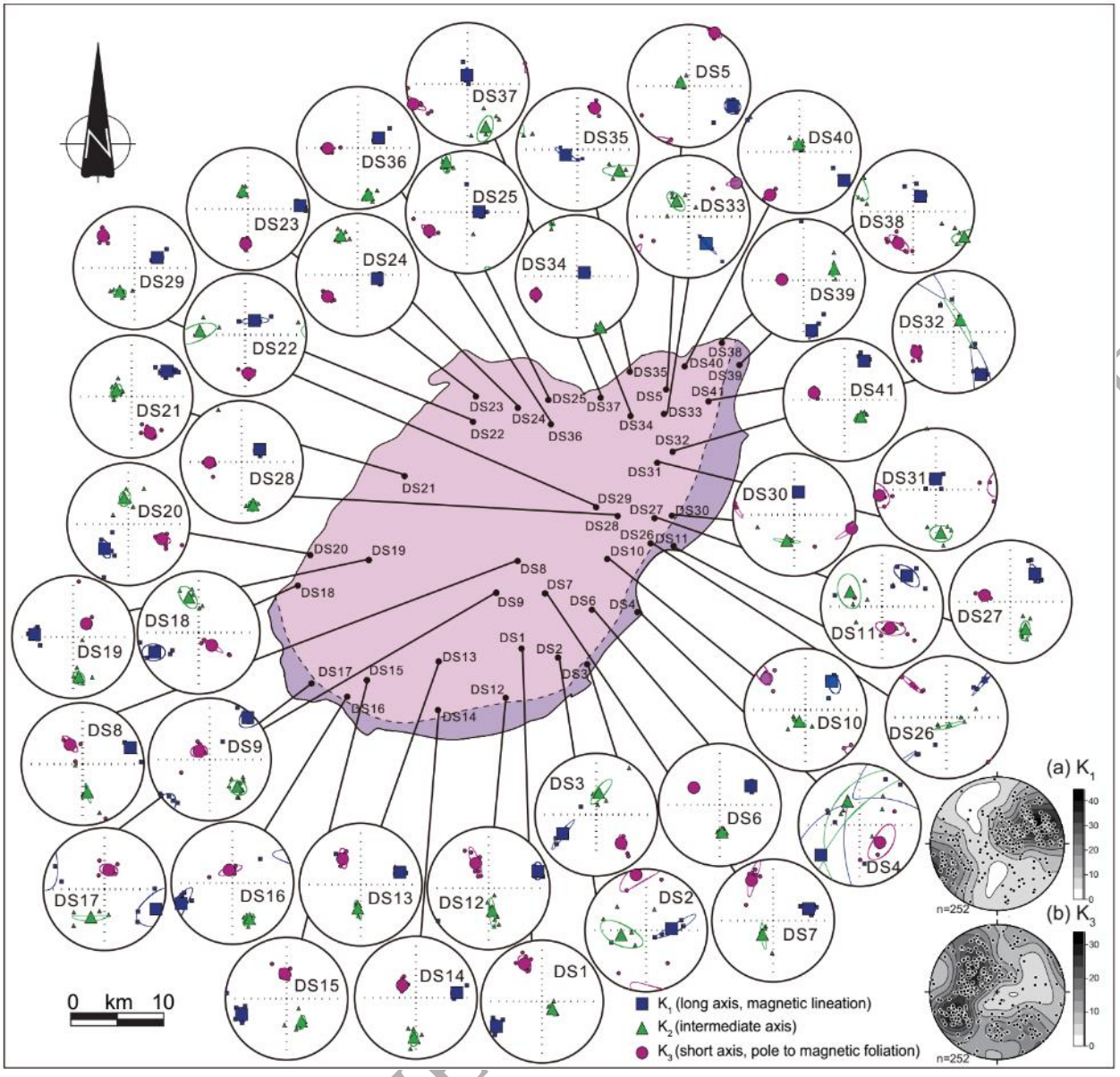

Figure 10. Equal-area projections (lower hemisphere) of AMS results for each sampling site. Confidence ellipses at 95% level are drawn around each average orientation direction. (a) K_1, long axis or magnetic lineation; (b) K_3, short axis or pole to magnetic foliation.

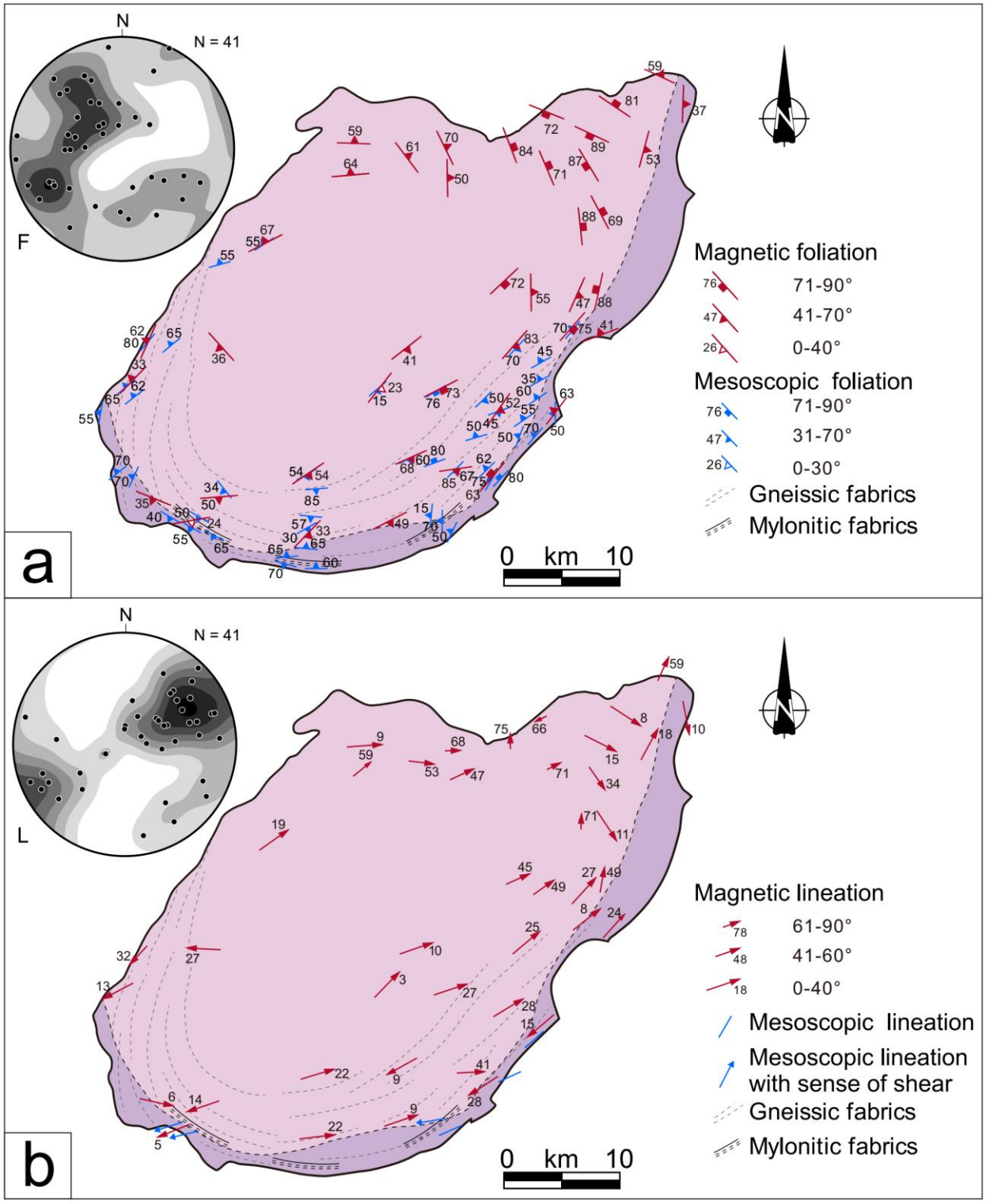

Figure 11. Mesoscopic and magnetic fabric patterns and orientation diagrams of K_3 and K_1. (a) Foliations. (b) Lineations.

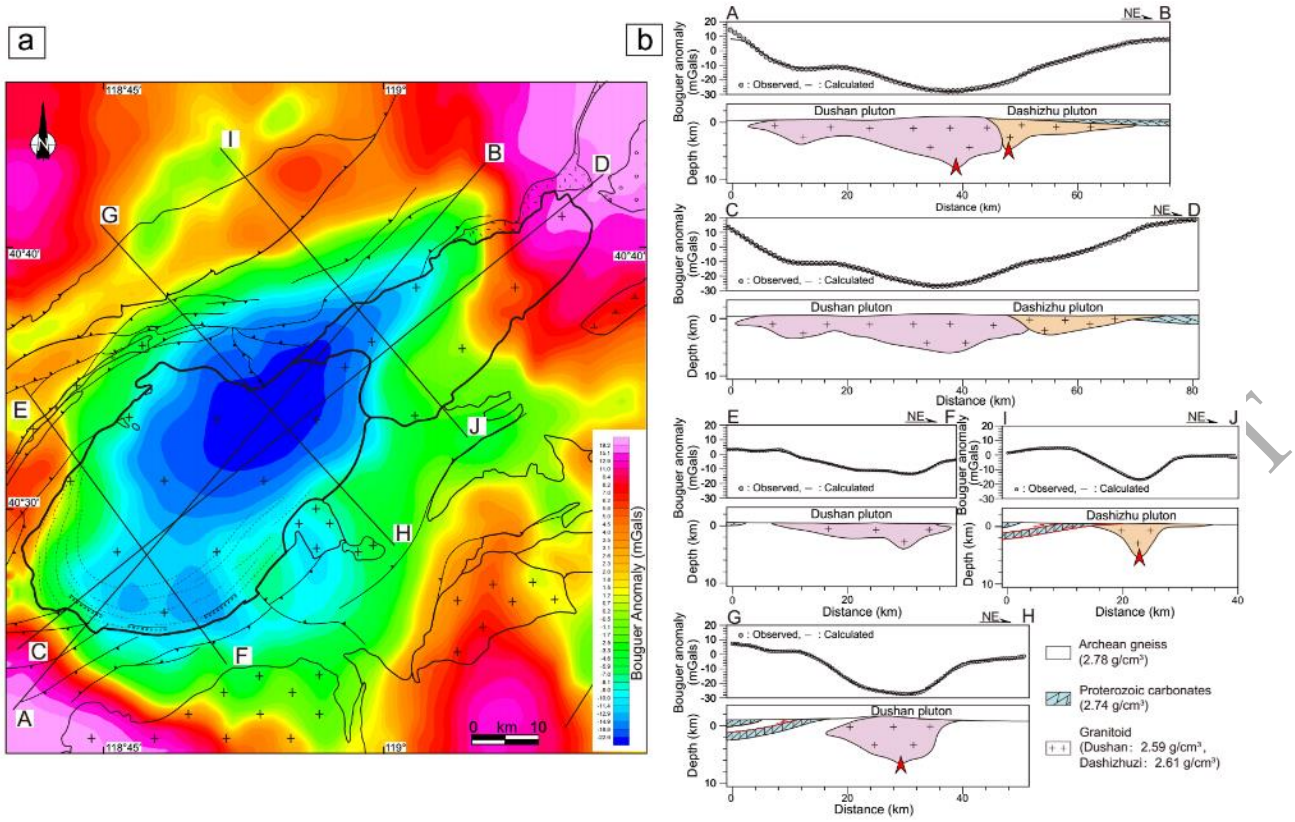

Figure 12. Gravity modeling. (a) Residual Bouguer gravity anomaly of the Dushan pluton and adjacent areas after subtraction of a 380 km wavelength regional trend from the complete Bouguer anomaly. Symbols and captions are the same as in Figure 2. (b) 2-D gravity modeling across the Dushan pluton. The arrows show the location of the possible feeder zones for the pluton.

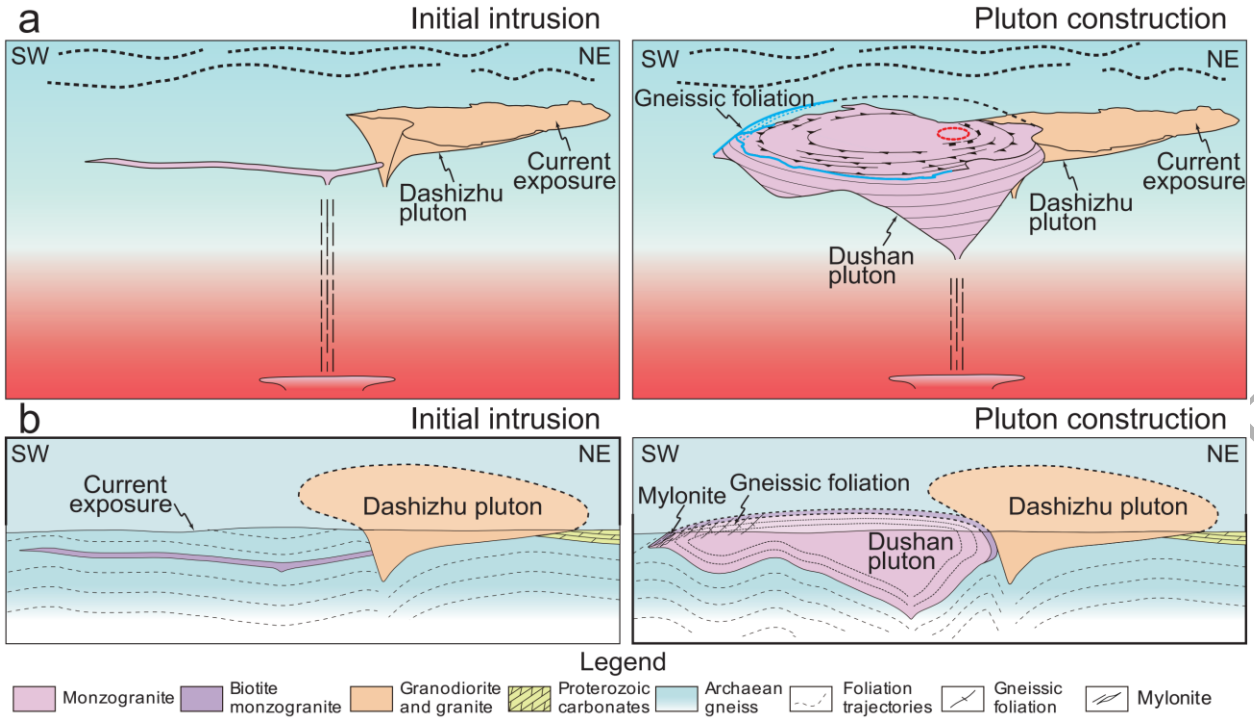

Figure 13. Fabric development mode of the Dushan pluton. (a) 3-D schematic sketch summarizing emplacement of the Dushan pluton. (b) Cross-sections of the Dushan pluton showing its emplacement. The overlying rocks above the current exposure are not considered, and the shape of the plutons at depth is inferred from gravity data.

Table 1. SIMS zircon U-Pb data of the collected samples in the Dushan pluton.

Sample spot	U (ppm)	Th (ppm)	Th/U	f_{206} (%)	$^{207}Pb/^{206}Pb$	±σ (%)	$^{207}Pb/^{235}U$	±σ (%)	$^{206}Pb/^{238}U$	±σ (%)	$t_{207/206}$(Ma)	±σ (Ma)	$t_{207/235}$(Ma)	±σ (Ma)	$t_{206/238}$(Ma)	±σ (Ma)
17DS39@01	458	384	0.838	0.54	0.05127	2.39	0.24552	2.82	0.0347	1.50	252.9	54.0	222.9	5.7	220.1	3.2
17DS39@02	400	350	0.875	0.05	0.05129	1.15	0.24534	1.90	0.0347	1.51	253.9	26.2	222.8	3.8	219.8	3.3
17DS39@03	802	312	0.390	0.27	0.05056	0.76	0.24451	1.69	0.0351	1.50	221.0	17.6	222.1	3.4	222.2	3.3
17DS39@04	783	107	0.136	1.60	0.05041	2.29	0.23715	2.75	0.0341	1.52	214.0	52.2	216.1	5.4	216.3	3.2
17DS39@05	191	67	0.351	0.29	0.05053	1.53	0.23646	2.26	0.0339	1.66	219.4	35.1	215.5	4.4	215.2	3.5
17DS39@06	2441	1537	0.630	0.53	0.05065	0.87	0.24537	1.73	0.0351	1.50	224.9	19.9	222.8	3.5	222.6	3.3
17DS39@07	147	178	1.214	0.17	0.05077	2.04	0.24631	2.54	0.0352	1.52	230.5	46.3	223.6	5.1	222.9	3.3
17DS39@08	534	94	0.175	0.15	0.05106	1.10	0.23923	1.87	0.0340	1.51	243.3	25.2	217.8	3.7	215.4	3.2
17DS39@09	143	47	0.328	0.08	0.05079	1.87	0.23834	2.41	0.0340	1.51	231.5	42.7	217.1	4.7	215.7	3.2
17DS39@10	617	299	0.484	0.42	0.04984	1.76	0.23266	2.32	0.0339	1.52	187.6	40.4	212.4	4.5	214.6	3.2
17DS39@11	106	66	0.622	0.33	0.05098	3.63	0.23855	3.93	0.0339	1.50	240.0	81.7	217.2	7.7	215.1	3.2
17DS39@12	406	92	0.227	0.09	0.05080	1.50	0.23475	2.12	0.0335	1.50	231.7	34.3	214.1	4.1	212.5	3.1
17DS39@13	386	327	0.845	0.13	0.05057	1.44	0.23618	2.11	0.0339	1.54	221.1	33.0	215.3	4.1	214.8	3.3
17DS39@14	322	279	0.867	0.11	0.05132	1.52	0.24182	2.14	0.0342	1.51	255.1	34.5	219.9	4.2	216.6	3.2
17DS39@15	294	213	0.724	0.26	0.04908	2.05	0.22575	2.55	0.0334	1.52	151.5	47.3	206.7	4.8	211.6	3.2
17DS39@16	1105	625	0.566	0.15	0.05055	0.81	0.24353	1.71	0.0349	1.50	220.3	18.6	221.3	3.4	221.4	3.3
17DS39@17	165	112	0.677	0.30	0.04927	2.92	0.23323	3.30	0.0343	1.52	160.6	67.0	212.9	6.3	217.6	3.3
17DS39@18	460	193	0.420	1.95	0.03938	3.98	0.18873	4.25	0.0348	1.50	-391.6	100.5	175.5	6.9	220.3	3.2
17DS39@19	489	83	0.170	3.21	0.03629	5.20	0.17597	5.41	0.0352	1.51	-608.9	136.0	164.6	8.3	222.8	3.3
17DS39@20	1017	668	0.657	0.17	0.05089	0.74	0.24850	1.68	0.0354	1.51	235.9	16.9	225.4	3.4	224.3	3.3
17DS39@21	329	122	0.372	0.26	0.05062	1.75	0.23601	2.31	0.0338	1.51	223.6	39.9	215.2	4.5	214.4	3.2
DS44@01	312	275	0.881	1.25	0.04591	3.65	0.21627	3.97	0.0342	1.56	-7.0	85.8	198.8	7.2	216.6	3.3
DS44@02	989	878	0.888	0.05	0.05102	0.72	0.25174	1.67	0.0358	1.50	241.5	16.6	228.0	3.4	226.7	3.4
DS44@03	408	678	1.659	2.13	0.04835	5.54	0.23308	5.75	0.0350	1.53	116.3	125.7	212.7	11.1	221.6	3.3
DS44@04	448	394	0.878	1.51	0.04388	3.33	0.22084	3.65	0.0365	1.51	-117.6	80.1	202.6	6.7	231.1	3.4
DS44@05	232	170	0.735	0.01	0.16591	1.20	10.51154	2.09	0.4595	1.71	2516.8	20.0	2480.9	19.6	2437.3	34.9
DS44@06	477	404	0.848	0.04	0.05062	1.53	0.24573	2.15	0.0352	1.51	223.7	34.9	223.1	4.3	223.0	3.3
DS44@07	424	304	0.717	0.29	0.05073	1.03	0.24606	1.84	0.0352	1.53	228.8	23.6	223.4	3.7	222.9	3.4
DS44@08	294	209	0.710	0.25	0.05124	1.23	0.24760	2.01	0.0350	1.58	251.8	28.1	224.6	4.0	222.0	3.5
DS44@09	592	452	0.764	0.00	0.05014	0.87	0.24491	1.73	0.0354	1.50	201.4	20.0	222.4	3.5	224.4	3.3
DS44@10	870	829	0.953	0.05	0.05149	0.82	0.25116	1.71	0.0354	1.50	262.9	18.7	227.5	3.5	224.1	3.3
DS44@11	597	598	1.001	0.81	0.04949	3.41	0.23931	3.73	0.0351	1.51	171.3	77.6	217.9	7.3	222.2	3.3
DS44@12	840	790	0.941	0.24	0.05097	1.33	0.25461	2.01	0.0362	1.50	239.4	30.5	230.3	4.1	229.4	3.4
DS44@13	692	1036	1.498	0.13	0.05100	1.07	0.25134	1.85	0.0357	1.50	240.9	24.5	227.7	3.8	226.4	3.3
DS44@14	631	455	0.721	0.06	0.05071	1.35	0.24163	2.03	0.0346	1.52	227.8	31.0	219.8	4.0	219.0	3.3
DS44@15	367	285	0.777	0.86	0.04900	2.57	0.23800	2.98	0.0352	1.52	147.8	59.1	216.8	5.8	223.2	3.3
DS44@16	599	533	0.890	0.10	0.05070	1.18	0.25136	1.91	0.0360	1.50	227.0	27.1	227.7	3.9	227.7	3.4
DS44@17	477	374	0.784	1.17	0.04743	2.60	0.23919	3.01	0.0366	1.52	70.7	60.7	217.8	5.9	231.6	3.5
DS44@18	407	395	0.971	0.08	0.04989	2.11	0.24221	2.59	0.0352	1.50	189.6	48.3	220.2	5.1	223.1	3.3
DS44@19	386	328	0.851	0.19	0.05143	1.07	0.25639	1.91	0.0362	1.58	260.1	24.3	231.8	4.0	229.0	3.6
DS44@20	1439	2154	1.497	0.28	0.05147	1.07	0.25868	1.87	0.0364	1.53	262.0	24.3	233.6	3.9	230.8	3.5
DS44@21	615	499	0.812	0.03	0.05143	0.87	0.25571	1.75	0.0361	1.52	260.0	19.9	231.2	3.6	228.4	3.4
DS44@22	574	468	0.815	0.49	0.04978	1.26	0.25056	1.97	0.0365	1.52	184.6	29.1	227.0	4.0	231.2	3.4

f_{206} (%) is the percentage of common ^{206}Pb in total ^{206}Pb

Table 2. The results of AMS measurements for the Dushan pluton. Lat: latitude, Long: longitude, N: number of cylinders measured in each site, Km: mean magnetic susceptibility, P_J and T: anisotropy degree and shape parameter, respectively, K_1 and K_3: magnetic lineation and pole of magnetic foliation, respectively, Inc: inclination, and Dec: declination, α_{95max} and α_{95min}: Jelinek's statistic confidence at 95% level (Jelinek, 1981) in degrees, respectively.

site	Coordinates		N	K_m	P_J	T	K_1				K_3			
	Long(°E)	Lat(°N)		(10^{-6}SI)			Dec(°)	Inc(°)	α_{95max}(°)	α_{95min}(°)	Dec(°)	Inc(°)	α_{95max}(°)	α_{95min}(°)
DS1	118.843	40.460	6	9930	1.373	-0.236	241.6	9.4	7.0	3.1	335.5	22.1	11.1	7.0
DS2	118.866	40.456	5	852	1.062	0.084	86.6	41.2	34.2	5.7	352.1	5.1	26.3	8.5
DS3	118.884	40.452	5	1610	1.07	0.518	241.6	28.0	24.7	3.3	136.0	26.8	10	4.6
DS4	118.919	40.476	6	2320	1.091	0.418	230.4	15.0	81.8	28.3	127.4	40.0	30.5	14.4
DS5	118.934	40.582	5	15700	1.2	0.336	115.1	14.5	9.6	8.6	25.0	0.6	8.6	4.6
DS6	118.888	40.478	7	6920	1.439	-0.152	59.2	28.1	5.2	2.1	304.9	37.6	4.5	2.5
DS7	118.859	40.486	6	6600	1.498	-0.211	71.6	27.0	8.9	4.8	332.5	17.3	22.3	4.4
DS8	118.841	40.501	5	9530	1.322	-0.28	70.7	10.6	10.4	0.3	328.4	48.7	16.8	6.5
DS9	118.827	40.486	9	7980	1.239	-0.121	44.0	3.0	13.8	8.9	307.5	65.1	14.8	10.2
DS10	118.897	40.502	5	4810	1.238	-0.205	42.7	25.2	6.6	4.2	309.6	6.6	13.3	5.7
DS11	118.938	40.506	5	4280	1.055	-0.074	39.0	24.0	19.9	9.6	159.8	49.0	24.4	10.8
DS12	118.832	40.436	7	757	1.08	-0.295	70.9	9.1	9.6	4.7	332.9	40.9	23.8	5.8
DS13	118.791	40.454	7	9270	1.254	0.132	72.7	21.7	6.5	3.9	325.7	36.4	15.1	5.9
DS14	118.791	40.431	6	2960	1.178	-0.083	83.0	22.1	7.9	3.5	313.6	57.4	9.4	5.3
DS15	118.746	40.445	7	1220	1.152	0.439	250.5	14.1	8.6	6.0	355.4	45.7	10.2	7.3
DS16	118.731	40.436	5	11000	1.182	0.201	248.2	5.4	22.3	6.3	350.4	66.0	21.8	6.4
DS17	118.712	40.444	5	411	1.048	0.199	111.0	6.0	24.6	15.5	12.4	54.7	15.6	9.5
DS18	118.702	40.490	5	2220	1.335	-0.122	246.0	13.6	13.3	9.5	134.3	56.8	21.1	3.5
DS19	118.746	40.502	8	9490	1.092	-0.525	274.1	27.0	8.4	3.3	48.4	53.9	7.5	3.3
DS20	118.708	40.505	7	397	1.066	-0.04	223.3	32.0	13.7	6.5	113.8	28.1	11.4	5.6
DS21	118.769	40.542	7	8760	1.415	0.624	54.8	18.5	12.1	4.7	152.8	22.7	9.5	5.0
DS22	118.812	40.567	5	1770	1.182	0.645	33.3	58.6	23.3	5.1	175.4	25.7	9.4	5.2
DS23	118.814	40.579	6	12700	1.5	0.553	86.4	9.1	5.2	3.7	181.9	31.1	6.8	3.9
DS24	118.841	40.573	8	15700	1.413	0.565	97.2	52.8	4.8	3.6	233.4	28.7	7.2	1.5
DS25	118.860	40.578	7	24800	1.264	0.502	87.8	67.8	10.9	4.3	244.1	20.5	10.6	3.2
DS26	118.925	40.510	5	13800	1.178	0.368	45.7	7.7	24.9	2.1	313.6	15.2	15.4	2.4
DS27	118.927	40.522	6	19900	1.334	-0.13	42.0	26.9	14.0	4.3	283.7	43.0	9.9	3.0
DS28	118.904	40.523	6	10900	1.319	-0.088	55.0	49.3	7.3	4.0	268.9	35.5	6.2	4.5
DS29	118.890	40.526	7	11700	1.309	-0.691	65.7	44.7	9.3	3.5	316.7	18.2	7.7	4.2
DS30	118.937	40.523	5	16200	1.287	-0.744	10.9	48.5	4.4	1.0	103.3	2.1	20.6	2.2
DS31	118.929	40.548	6	9540	1.328	0.546	1.7	71.0	12.6	8.0	264.3	2.5	14.2	10.2
DS32	118.938	40.552	6	1060	1.099	0.471	147.4	11.1	45.3	8.6	241.6	20.6	9.2	4.4
DS33	118.932	40.568	5	5360	1.164	0.202	146.9	34.4	19.5	1.6	54.8	3.0	10.5	2.5
DS34	118.912	40.569	7	14200	1.419	0.468	64.1	71.4	5.6	3.2	245.6	18.6	4.3	3.1
DS35	118.911	40.591	5	9100	1.202	0.585	245.4	66.4	22	4.4	22.6	17.7	7.7	4.6
DS36	118.862	40.566	7	16900	1.394	0.289	64.7	47.4	8.7	5	269.1	39.9	8.2	3.5
DS37	118.894	40.578	8	4690	1.148	0.212	359.4	74.5	14.3	3.8	248.9	5.6	12.5	3.3
DS38	118.970	40.607	8	22200	1.084	0.172	25.0	59.2	10.1	7.5	205.3	30.8	16.7	6.7
DS39	118.982	40.594	7	17900	1.27	0.713	168.4	10.3	1.03	1.8	272.3	52.9	4.4	2.2
DS40	118.947	40.593	5	14400	1.179	0.479	122.5	8.1	9.7	3.0	213.8	9.5	7.5	1.2
DS41	118.961	40.576	5	23400	1.345	0.733	28.7	18.3	7.6	3.1	284.5	36.6	7.9	0.9